Marine Structures 72 (2020) 102771

Contents lists available at ScienceDirect

Marine Structures

journal homepage: http://www.elsevier.com/locate/marstruc

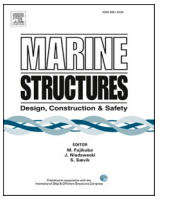

Integrated design optimization of spar floating wind turbines

John Marius Hegseth [a,*], Erin E. Bachynski [a], Joaquim R.R.A. Martins [b]

[a] Department of Marine Technology, NTNU, 7491, Trondheim, Norway
[b] Department of Aerospace Engineering, University of Michigan, Ann Arbor, MI, 48109, USA

ARTICLE INFO

Keywords:
Offshore wind energy
Floating wind turbines
Integrated design
Gradient-based optimization

ABSTRACT

A linearized aero-hydro-servo-elastic floating wind turbine model is presented and used to perform integrated design optimization of the platform, tower, mooring system, and blade-pitch controller for a 10 MW spar floating wind turbine. Optimal design solutions are found using gradient-based optimization with analytic derivatives, considering both fatigue and extreme response constraints, where the objective function is a weighted combination of system cost and power quality. Optimization results show that local minima exist both in the soft-stiff and stiff-stiff range for the first tower bending mode and that a stiff-stiff tower design is needed to reach a solution that satisfies the fatigue constraints. The optimized platform has a relatively small diameter in the wave zone to limit the wave loads on the structure and an hourglass shape far below the waterline. The shape increases the restoring moment and natural frequency in pitch, which leads to improved behaviour in the low-frequency range. The importance of integrated optimization is shown in the solutions for the tower and blade-pitch control system, which are clearly affected by the simultaneous design of the platform. State-of-the-art nonlinear time-domain analyses show that the linearized model is conservative in general, but reasonably accurate in capturing trends, suggesting that the presented methodology is suitable for preliminary integrated design calculations.

1. Introduction

Floating wind turbines (FWTs) are complex multidisciplinary systems, which makes design optimization a challenging and time consuming task. Different components, such as the wind turbine control system, tower, platform, and mooring system, are typically designed separately in a sequential manner; however, due to strong coupling between the disciplines, this often leads to suboptimal solutions at the overall system level. It is therefore desirable to use an integrated optimization approach where the components are designed simultaneously while considering all relevant disciplines. Multidisciplinary design optimization (MDO) techniques can be used to solve such problems [1].

A large body of literature exists on the topic of FWT design, often using parametric studies to assess the behaviour of the system. Tracy [2] performed simplified frequency-domain analyses to evaluate a large variety of FWT designs. Bachynski and Moan [3] used spreadsheet calculations together with fully coupled time-domain simulations to analyse different design parameters for five tension leg platform (TLP) wind turbines. Gilloteaux and Bozonnet [4] examined the response of cylinder-shaped FWTs with different geometries.

An early study on hydrodynamic shape optimization of offshore structures using computer-aided optimization was carried out by

* Corresponding author.
E-mail address: john.m.hegseth@ntnu.no (J.M. Hegseth).

https://doi.org/10.1016/j.marstruc.2020.102771
Received 5 November 2019; Received in revised form 29 March 2020; Accepted 30 March 2020
Available online 30 April 2020

Clauss and Birk [5], and more recently, these techniques have also been applied in the design of FWT systems. Brommundt et al. [6] optimized the catenary mooring system for a semi-submersible FWT using frequency-domain analyses. The model included the directionality of the environmental loads and thus also considered the layout of the mooring lines. Hall et al. [7] performed single- and multi-objective hull shape and mooring line optimization for different platform concepts spanning all stability classes and found that the Pareto front was dominated by relatively complex platforms with several legs and taut mooring lines. The work was later extended by Karimi et al. [8], using an updated dynamic model and a new optimization algorithm, which significantly affected the derived optimal solutions. Myhr and Nygaard [9] used time-domain simulations and two extreme load cases to optimize the structural design of a tension leg buoy and found that the wave forces could be significantly reduced if the cylindrical platform section in the wave zone was replaced with a space frame. Muskulus and Schafhirt [10] offers a comprehensive review of wind turbine support structure optimization.

Despite gradient-based optimization being desirable due to its efficiency, especially for large design spaces [10], most of the work on FWT design optimization has been performed using gradient-free methods. This is likely due to the difficult task of computing accurate gradients. One exception is Fylling and Berthelsen [11], who optimized the hull shape, mooring lines and power cable for a spar FWT using a gradient-based approach with numerical gradients obtained using finite differences.

The aforementioned studies consider the design of the platform, mooring system, or both, but the tower, rotor, and control system are considered fixed during the optimization. Because the design process must consider the energy production and not only the cost of the FWT system, the control system should preferably be integrated in the optimization procedure [12]. Numerical optimization of a land-based wind turbine controller has been performed by Tibaldi et al. [13], but little exists in the literature concerning FWTs. A first step in this direction was made by Lemmer et al. [14], who optimized four main dimensions of a three-column semi-submersible FWT, where the controller was automatically tuned in each design iteration using a linear quadratic regulator (LQR). The optimization sought to minimize a combination of material costs and damage-equivalent loads in the tower for seven operational conditions, with a constraint on the static pitch angle at rated thrust.

A limitation of previous work on FWT design optimization is that the large-volume platform is considered rigid in the design analyses. In addition, the tower design is typically not considered in the optimization process. Since turbines are getting larger, the flexibility of the platform is becoming increasingly important and may need to be considered to obtain the correct global behaviour of the system. The elasticity of the platform affects both the shape and the natural frequency of the structure's eigenmodes, which may influence the tower response.

To address these issues, the current work develops an integrated optimization process that considers the tower and platform design simultaneously, and captures the coupling effects between the two subsystems. A flexible hull, combined with distributed hydrodynamic forces, also enables the structural design of the platform to be integrated in the global optimization loop. A computationally efficient low-fidelity model is used to analyse the linearized aero-hydro-servo-elastic dynamics of a 10 MW spar FWT in the frequency domain. The model is implemented in the OpenMDAO framework [15], which enables efficient gradient-based optimization using analytic gradients. The spar platform, tower, mooring system, and control system are then optimized in an integrated fashion, considering both fatigue and extreme response constraints, where a weighted combination of system cost and power quality is employed as the objective function. Finally, the results are verified against nonlinear time-domain analyses. The rotor design is not modified during the optimization, since the model is considered unsuitable for local blade response. The design optimization of wind turbine rotors is considered to be outside the scope of the current work, but has been considered separately [16–18].

Since the presented design optimization methodology is based on a simplified dynamic model, its main purpose is to help designers in the preliminary design phase. Due to the computational efficiency of the model, it can also be used to quickly get insight into the system behaviour, and to study the effect of changes in system parameters on the dynamic response and resulting design solutions. Detailed design would require more accurate nonlinear analyses incurring a much greater computational cost.

The paper is organized as follows. The linear FWT model used to perform the integrated design analyses is presented in Section 2. In Section 3, the optimization problem is summarized and the design variables, constraints, and objective function are described in detail. The results from the optimization study are presented and discussed in Section 4, and the optimized design solutions are verified using a high-fidelity simulation tool. Finally, the findings are summarized in Section 5.

2. FWT model

The coupled dynamics of FWTs are typically analysed using nonlinear time-domain analyses, which capture the complex interactions between aerodynamics, hydrodynamics, structural dynamics, and control. For a design optimization procedure that requires several iterations to converge, each involving a large number of load cases, the process becomes computationally prohibitive. Simplified models are therefore needed, especially in the conceptual design phase, where large parts of the design space are explored to identify possible solutions.

The present design optimization study considers a spar buoy that supports the DTU 10 MW reference wind turbine [19] at a water depth of 320 m. The steel hull is partially filled with concrete ballast to achieve the correct draft, using a ballast density of 2600 kg/m^3. The interface with the tower is located 10 m above the still water line (SWL), while the hub height is 119 m above the SWL. A catenary mooring system consisting of three lines spread symmetrically about the vertical axis is used for station-keeping. For simplicity, the so-called crowfeet (or delta lines) are removed, and lines with constant cross-sectional properties are used. The yaw motions of the platform are not included in the linearized model.

Only the response in the x-z-plane is considered in the current work, and co-directional waves and wind travelling in the positive x-direction are applied in all simulations. An overview of the FWT system, including the mooring system layout, is shown in Fig. 1.

2.1. Linearized system formulation

The system is linearized to obtain the equations of motion, which are solved in the frequency domain. The model is expressed in state-space form, and consists of a structural part and a control system part, which are connected to obtain the complete closed-loop aero-hydro-servo-elastic model in Section 2.4. The linearized system considers perturbations in the state and input variables, **x** and **u** respectively, about the operational point:

$$\mathbf{x} = \mathbf{x}_0 + \Delta\mathbf{x}, \quad \mathbf{u} = \mathbf{u}_0 + \Delta\mathbf{u}. \tag{1}$$

The dynamic equations of motion are then expressed as

$$\Delta\dot{\mathbf{x}} = \mathbf{A}\Delta\mathbf{x} + \mathbf{B}\Delta\mathbf{u}, \tag{2}$$

where **A** is the state matrix, and **B** is the input matrix. In the rest of this work, the Δ sign is omitted for brevity.

2.2. Structural model

2.2.1. Platform and turbine

The structural model for the platform and turbine considers four degrees-of-freedom (DOFs), as shown in Fig. 2. The equations of motion for the three support structure DOFs (surge, pitch, and the first bending mode of the tower and platform) are derived by using generalized displacements similar to Hegseth and Bachynski [20], but using a flexible hull. Hydrodynamic excitation loads are found from MacCamy–Fuchs theory, while the added mass is based on analytical 2D coefficients. Radiation damping is neglected, while viscous damping is computed using a stochastic linearization of the drag term in Morison's equation. The three support structure DOFs are gathered in the vector $\boldsymbol{\xi} = [\xi_1 \quad \xi_5 \quad \xi_7]^\top$. The differential equation for the rotor speed, $\dot{\phi}$, considers only rigid body dynamics and thus neglects the torsional DOF of the shaft:

$$I_D\,\ddot{\phi} = Q_A - N_{gear}Q_G. \tag{3}$$

Here, I_D is the rotor and drivetrain inertia, Q_A is the aerodynamic torque, N_{gear} is the gear ratio, and Q_G is the generator torque.

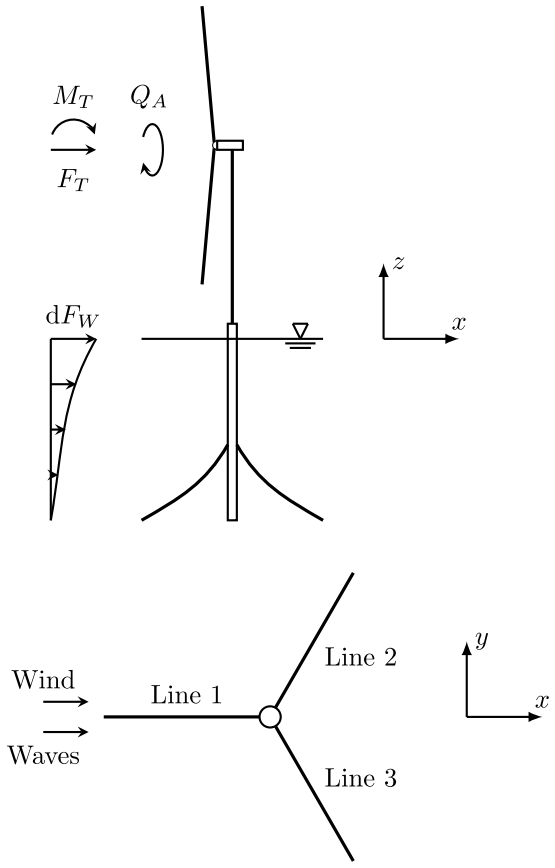

Fig. 1. Overview of the FWT system.

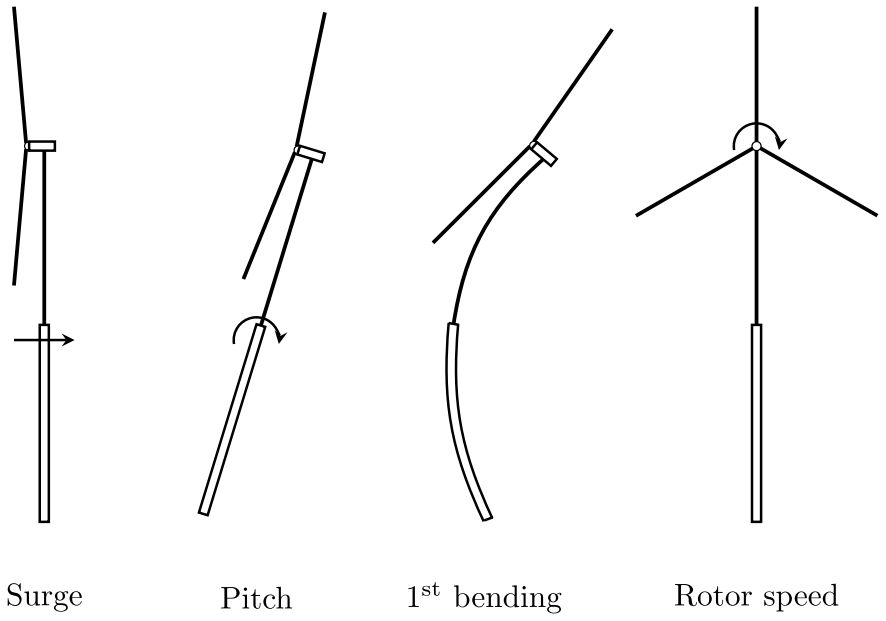

Fig. 2. Structural DOFs considered in the model.

For each wind-wave condition, the linearization point for the system is found from static equilibrium when the system is subjected to the mean environmental loads. In addition to the mean aerodynamic loads on the rotor, the static component of the aerodynamic quadratic drag force on the tower is included.

Although the linearized model presented here may yield reasonably accurate estimates for the global response of the tower, platform and mooring lines, it is not considered suitable for blade design, which typically involves nonlinear analyses in the time domain. One exception is Merz [21], who performed conceptual blade design for a stall-regulated offshore wind turbine using linear frequency-domain analyses. Because modern wind turbine blades are made of composite materials, and because they are more sensitive to local aerodynamic effects than the support structure and mooring system, including the blade design would require significant enhancements to the aerodynamic and structural models presented here, which is outside the scope of the current work. In addition, previous studies on FWTs have indicated that transient fault conditions, which cannot be analysed with the presented methodology, may be critical for extreme blade loads [22,23]. The blade response is therefore not considered in the model; instead, the aerodynamic forces are applied as resultant loads on the tower top.

With the structural DOFs described above, the state vector is defined as

$$\mathbf{x}_s = \begin{bmatrix} \boldsymbol{\xi} \\ \dot{\boldsymbol{\xi}} \\ \dot{\boldsymbol{\phi}} \end{bmatrix}. \tag{4}$$

The inputs to the structural system consist of both control system outputs and disturbances due to environmental loads, which are separated in two different vectors $\mathbf{u}_{sc}$ and $\mathbf{u}_{sd}$. The control input vector is written as

$$\mathbf{u}_{sc} = \begin{bmatrix} Q_G \\ \theta \end{bmatrix}, \tag{5}$$

where θ is the collective blade pitch angle, which is found from the control system model, together with the generator torque. The current implementation neglects the dynamics of the generator and pitch actuator systems, and the generator torque and blade pitch are thus instantaneously set to their reference values at each time step.

The wind speed varies over the rotor disk; however, because only the resultant aerodynamic loads at the tower top are of interest in the analysis, it is desirable to express the wind input using a single scalar variable. This is achieved by expressing a rotor effective wind speed for each of the three resultant forces in Fig. 1. The rotor effective wind speed is a spatially constant wind speed that yields the same resultant forces on the rotor as the full wind field and may therefore be considered as a weighted average of the wind speed seen by the different blade elements. The disturbance vector is expressed as

$$\mathbf{u}_{sd} = \begin{bmatrix} v_{F_T} & v_{M_T} & v_{Q_A} & F_{W,1} & F_{W,5} & F_{W,7} \end{bmatrix}^\top, \tag{6}$$

where v_{F_T}, v_{M_T} and v_{Q_A} are the effective wind speeds for thrust, tilting moment and aerodynamic torque, respectively, which are derived in Section 2.5.2. $F_{W,n}$ represents the generalized wave excitation force in support structure DOF n, found from MacCamy–Fuchs theory. The resulting system is written as:

$$\dot{\mathbf{x}}_s = \mathbf{A}_s\mathbf{x}_s + \mathbf{B}_{sc}\mathbf{u}_{sc} + \mathbf{B}_{sd}\mathbf{u}_{sd}, \tag{7a}$$

$$\mathbf{y}_s = \mathbf{C}_s\mathbf{x}_s, \tag{7b}$$

where the state matrix is found from the total mass (**M**, including hydrodynamic added mass), stiffness (**K**), and damping (**D**) matrices for the system

$$\mathbf{A}_s = \begin{bmatrix} \mathbf{0} & \mathbf{I} \\ -\mathbf{M}^{-1}\mathbf{K} & -\mathbf{M}^{-1}\mathbf{D} \end{bmatrix} \tag{8}$$

The input matrices $\mathbf{B}_{sc}$ and $\mathbf{B}_{sd}$ relate control inputs and disturbances to forces on the structural DOFs, while the output matrix for the structural model, $\mathbf{C}_s$, is chosen such that the rotor speed is the single output to match the control system input:

$$\mathbf{C}_s = [0 \quad 0 \quad 0 \quad 0 \quad 0 \quad 0 \quad 1]. \tag{9}$$

2.2.2. Mooring system

The response of the mooring lines is calculated using the simplified dynamic frequency-domain model described by Larsen and Sandvik [24] and later extended by Lie and Sødahl [25]. Here, the lines are modelled as a single DOF system, as shown in Fig. 3.

The dynamic tension in the line can then be derived as

$$T_D = k_E[x(t) - u(t)] = c^*|\dot{u}(t)|\dot{u}(t) + k_G u(t) + \omega^2 m^* x(t), \tag{10}$$

where $u(t)$ is the generalized displacement of the line, found from a quasi-static analysis where the upper end is displaced two times the standard deviation of the platform motion from the equilibrium position (significant motion). The geometric stiffness (k_G) is found as the secant stiffness when the line is moved from equilibrium to the position of significant motion. The generalized inertia coefficient (m^*) and damping coefficient (c^*) are found using the quasi-static line configuration as the shape function. The linearized damping coefficient (c_L) is computed using the stochastic linearization

$$c^*|\dot{u}(t)|\dot{u}(t) \approx c^*\sqrt{\frac{8}{\pi}}\sigma_{(\dot{u})}\dot{u}(t) = c_L\dot{u}(t), \tag{11}$$

where $\sigma_{(\dot{u})}$ denotes the standard deviation of $\dot{u}$. Because Eq. (10) can be considered to be a variant of Morison's equation, non-Gaussian extremes for the dynamic mooring line tension can be found from the normalized maxima distribution of the Morison force, which consists of a Rayleigh distribution for low probability levels and an exponential distribution for high probability levels [25]:

$$F_Y(y) = \begin{cases} 1 - \exp\left[-\left(3k^2+1\right)\dfrac{y^2}{2}\right], & 0 \le y \le y_0 \\ 1 - \exp\left[-\dfrac{\sqrt{3k^2+1}}{2k}\left(y - \dfrac{y_0}{2}\right)\right], & y \ge y_0, \end{cases} \tag{12}$$

where $y = T_D/\sigma_{(T_D)}$ is the normalized tension, and

$$y_0 = \frac{1}{2k\sqrt{3k^2+1}}. \tag{13}$$

The parameter k is a measure of the relative importance of drag and inertia forces.

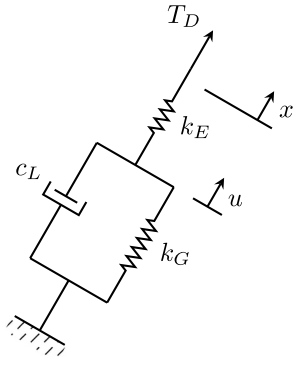

Fig. 3. Simplified dynamic mooring line model as illustrated by Lie and Sødahl [25].

2.3. Control system model

The baseline linear control system follows the generic approach for variable-speed pitch-controlled wind turbines [26]. The approach uses two independent controllers: a generator-torque controller for below-rated wind speeds and a collective blade-pitch controller for above-rated wind speeds. Typically, these types of controllers also include transition strategies to ensure smooth switchovers between regions; however, for simplicity, this is not included in the current implementation. In both control regimes, the control system is described with the following first-order system

$$\dot{\mathbf{x}}_c = \mathbf{A}_c\mathbf{x}_c + \mathbf{B}_c\mathbf{u}_c, \tag{14a}$$

$$\mathbf{y}_c = \mathbf{C}_c\mathbf{x}_c, \tag{14b}$$

where the rotor speed is the only input, and the outputs are the generator torque and the blade pitch angle:

$$\mathbf{u}_c = [\dot{\phi}], \quad \mathbf{y}_c = \begin{bmatrix} Q_G \\ \theta \end{bmatrix}. \tag{15}$$

First, the rotor speed is filtered through a first-order low-pass filter with corner frequency ω_{lp} to avoid high-frequency excitation of the control system

$$\mathbf{A}_c = \begin{bmatrix} 0 & 1 \\ 0 & -\omega_{lp} \end{bmatrix}, \quad \mathbf{B}_c = \begin{bmatrix} 0 \\ \omega_{lp} \end{bmatrix}, \quad \mathbf{x}_c = \begin{bmatrix} \phi_{lp} \\ \dot{\phi}_{lp} \end{bmatrix}, \tag{16}$$

where $\dot{\phi}_{lp}$ is the low-pass filtered rotor speed. Below the rated wind speed, the generator torque is set to be proportional to the square of the rotor speed to balance the aerodynamic torque and thus maintain the optimal tip-speed ratio, which maximizes the power output. Above the rated wind speed, the generator torque is kept constant at the rated torque, and a PI controller is used to modify the collective blade pitch angle:

$$\mathbf{C}_c = \begin{bmatrix} 0 & 2K\dot{\phi}_0 \\ 0 & 0 \end{bmatrix} (\text{below rated}), \tag{17}$$

$$\mathbf{C}_c = \begin{bmatrix} 0 & 0 \\ \eta_k k_i & \eta_k k_p \end{bmatrix} (\text{above rated}).$$

Here, K is the generator torque constant, η_k is the gain-scheduling parameter, while k_i and k_p are the integral and proportional gains of the PI controller, respectively.

2.4. Closed-loop system

The structural and control system models can be written as a single closed-loop system by setting $\mathbf{y_s} = \mathbf{u_c}$ and $\mathbf{u}_{sc} = \mathbf{y_c}$:

$$\dot{\mathbf{x}} = \mathbf{A}\mathbf{x} + \mathbf{B}\mathbf{u}_{sd}, \tag{18a}$$

$$\mathbf{y} = \mathbf{C}\mathbf{x}, \tag{18b}$$

where

$$\mathbf{A} = \begin{bmatrix} \mathbf{A}_s & \mathbf{B}_{sc}\mathbf{C}_c \\ \mathbf{B}_c\mathbf{C}_s & \mathbf{A}_c \end{bmatrix}, \quad \mathbf{B} = \begin{bmatrix} \mathbf{B}_{sd} \\ \mathbf{0} \end{bmatrix}, \quad \mathbf{x} = \begin{bmatrix} \mathbf{x_s} \\ \mathbf{x_c} \end{bmatrix}, \tag{19}$$

and $\mathbf{C}$ is set to the identity matrix. The closed-loop system is then transformed to the frequency domain. The transfer matrix between disturbances and outputs for a frequency ω is defined as:

$$\mathbf{H}(\omega) = \mathbf{C}(i\omega\mathbf{I} - \mathbf{A})^{-1}\mathbf{B}. \tag{20}$$

The cross-spectral density matrix of the response vector $\mathbf{y}$ can be calculated from

$$\mathbf{S}_\mathbf{y}(\omega) = \mathbf{H}(\omega)\mathbf{S}_\mathbf{u}(\omega)\mathbf{H}(\omega)^H, \tag{21}$$

where $(\cdot)^H$ denotes the conjugate transpose [27]. The variance spectra of $\mathbf{y}$ are then found along the diagonal of $\mathbf{S}_\mathbf{y}(\omega)$.

The cross spectral density matrix ($\mathbf{S}_\mathbf{u}(\omega)$) is used for the load process and has the following structure

$$\mathbf{S}_\mathbf{u}(\omega) = \begin{bmatrix} \mathbf{S}_{\text{wind}}(\omega) & \mathbf{0} \\ \mathbf{0} & \mathbf{S}_{\text{wave}}(\omega) \end{bmatrix} \tag{22}$$

The off-diagonal terms above are zero because the wind and wave processes are assumed to be uncorrelated [28].

The resulting response spectra are applied, together with dynamic equilibrium, to find the bending moment response along the

tower and platform. The fatigue damage is then calculated at selected locations using the Dirlik method [29].

The extreme response of the support structure is computed using the average upcrossing rate (AUR) method [30]. Assuming that the response process is stationary and Gaussian with zero mean, the cumulative distribution function (CDF) of the extreme value Y for an arbitrary response parameter can be written as [27].

$$F_Y(y) = \exp\left\{ -\nu^+(0)\, T \exp\left(-\frac{y^2}{2\sigma^2} \right) \right\}, \tag{23}$$

where $\nu^+(0)$ is the mean zero-upcrossing rate, which can be found from the zeroth- and second-order spectral moments:

$$\nu^+(0) = \frac{1}{2\pi} \sqrt{\frac{m_2}{m_0}}. \tag{24}$$

The n^{th} spectral moment is defined as:

$$m_n = \int_0^\infty \omega^n S(\omega) \mathrm{d}\omega. \tag{25}$$

The most probable maximum value in 1 h, y_{1h}, is used in the design constraints related to extreme response. The value is approximated using:

$$F_Y(y_{1h}) = \mathrm{e}^{-1}. \tag{26}$$

The mean value of the response process is then added to y_{1h} to obtain the total extreme value. We have used this methodology to compute fatigue damage in the tower base, as well as extreme surge, pitch, and tower base bending moment response, for two 10 MW spar FWT designs in previous work [20]. We found this methodology to yield good agreement within ± 30% for long-term fatigue and ± 15% for short-term extremes when compared to nonlinear time-domain simulations.

2.5. Aerodynamic forces

2.5.1. Linearized BEM theory

The aerodynamic forces on the blades are computed using blade-element momentum (BEM) theory [31,32]. A quasi-steady formulation is used, meaning that dynamic wake and dynamic stall effects are neglected. The Glauert correction and hub and tip loss factors are included in the model. The normal and tangential inflow velocities for a blade section at radius r are defined as:

$$V_n = v\,(1 - a_n), \tag{27a}$$

$$V_t = \dot{\phi}\, r\,(1 + a_t), \tag{27b}$$

where v is the relative wind speed, and a_n and a_t are the normal and tangential induction factors, respectively. In the analyses, induction factors for the different blade sections are found from pre-calculated lookup tables as functions of blade pitch angle and tip speed ratio. The inflow velocity W and inflow angle φ seen by the blade element are then expressed as

$$W = \sqrt{V_n^2 + V_t^2}, \tag{28a}$$

$$\varphi = \tan^{-1}\frac{V_n}{V_t}. \tag{28b}$$

The angle of attack is the difference between the inflow angle and the element's combined pitch and twist angle:

$$\alpha = \varphi - (\theta + \beta). \tag{29}$$

Here, β is the twist angle. The lift and drag forces can then be computed using tabulated lift and drag coefficients

$$L = \frac{1}{2}\rho c W^2 C_l(\alpha), \tag{30a}$$

$$D = \frac{1}{2}\rho c W^2 C_d(\alpha). \tag{30b}$$

The normal and tangential forces relative to the rotor plane are found from a coordinate system transformation

$$F_n = L\cos\varphi + D\sin\varphi \tag{31a}$$

$$F_t = L\sin\varphi - D\cos\varphi. \tag{31b}$$

The blade root loads of interest, i.e., the flapwise shear force F_y, the flapwise bending moment M_z, and the edgewise bending moment M_y, are found by integrating the loads over the length of the blade

$$F_y = \int_0^R F_n \, \mathrm{d}r, \tag{32a}$$

$$M_z = \int_0^R r \, F_n \, \mathrm{d}r, \tag{32b}$$

$$M_y = \int_0^R r \, F_t \, \mathrm{d}r. \tag{32c}$$

As seen in Eqs. (27)–(32), the aerodynamic forces are nonlinear functions of wind speed, rotor speed, and blade pitch angle. To obtain linear forces that can be applied in the simplified FWT model, the blade root forces are linearized using a first order Taylor expansion:

$$F_y \approx F_{y0} + F_{y,v}\Delta v + F_{y,\dot{\phi}}\Delta\dot{\phi} + F_{y,\theta}\Delta\theta, \tag{33a}$$

$$M_z \approx M_{z0} + M_{z,v}\Delta v + M_{z,\dot{\phi}}\Delta\dot{\phi} + M_{z,\theta}\Delta\theta, \tag{33b}$$

$$M_y \approx M_{y0} + M_{y,v}\Delta v + M_{y,\dot{\phi}}\Delta\dot{\phi} + M_{y,\theta}\Delta\theta, \tag{33c}$$

where the subscripts after the commas denote partial derivative with respect to the variable, i.e.,

$$A_{x,y} = \frac{\partial A_x}{\partial y}. \tag{34}$$

2.5.2. Rotor effective wind speed

A rotor effective wind speed is used to describe the incoming wind field. The effective wind speed is dependent on the type of resultant load (thrust force, tilting moment, or aerodynamic torque), as well as the mean wind speed.

As shown by Halfpenny [33], the (single sided) cross-spectral density of the rotationally sampled wind speed for two blade elements j and k can be written as:

$$S_v^{(jk)}(\omega) = \sum_{n=-\infty}^{\infty} \mathrm{e}^{in\psi} K_n^{(jk)}(|\omega - n\dot{\phi}|)\, S_U(|\omega - n\dot{\phi}|), \tag{35}$$

where $S_U(\omega)$ is the incoming wind spectrum, ψ is the azimuth angle between the elements, and K_n is the n^{th} Fourier coefficient of the coherence function γ, which is Fourier expanded in the rotor plane:

$$K_n^{(jk)}(\omega) = \frac{1}{\pi}\int_0^{\pi} \gamma\left(\omega, d_{jk}\right) \cos(n\theta)\, \mathrm{d}\theta. \tag{36}$$

The coherence function for two points with separation distance d and frequency f (in Hz) is taken from IEC [34] and expressed as

$$\gamma(f,d) = \exp\left(-12\left[\left(\frac{fd}{U_{\mathrm{hub}}}\right)^2 + \left(\frac{0.12d}{L_c}\right)^2\right]^{0.5}\right), \tag{37}$$

where U_{hub} is the mean hub-height wind speed and L_c is a coherence scale parameter.

The forces on each blade element can then be found from the rotationally sampled wind speed and weight factors relating wind speed to forces on the element. These weight factors are the partial derivatives of the blade element forces in Eq. (31) with respect to wind speed. When summing the forces on the blade elements to obtain the total tower top loads, cancellation of harmonics results in peaks at multiples of three of the rotor frequency (i.e., 3P, 6P, 9P, etc.) for the resultant force spectra. In the current work, harmonics higher than 3P are neglected. Tower shadow and wind shear are not included.

The spectra for the effective wind speeds are calculated from the resultant force spectra and the total weight factors over the rotor:

$$S_{v_{F_T}}(\omega) = \frac{S_{F_T}(\omega)}{\left(3\, F_{y,v}\right)^2}, \tag{38a}$$

$$S_{v_{M_T}}(\omega) = \frac{S_{M_T}(\omega)}{\left(\frac{3}{2}\, M_{z,v}\right)^2}, \tag{38b}$$

$$S_{v_{Q_A}}(\omega) = \frac{S_{Q_A}(\omega)}{\left(3\, M_{y,v}\right)^2}. \tag{38c}$$

The wind load submatrix in Eq. (22), $\mathbf{S}_{\mathrm{wind}}(\omega)$, can then be found simply by observing which harmonics of the wind are shared by

the different load components. As shown by Halfpenny [33], the thrust force and aerodynamic torque on the turbine are perfectly correlated, since they share all harmonics, and completely uncorrelated from the tilting moment. This is because they have no harmonics in common.

2.5.3. Resultant aerodynamic forces

Following the derivation of weight factors in the previous section, the relation between derivatives of the blade root forces and resultant forces on the rotor becomes evident:

$$F_{T,v} = 3\, F_{y,v}, \tag{39a}$$

$$M_{T,v} = \frac{3}{2}\, M_{z,v}, \tag{39b}$$

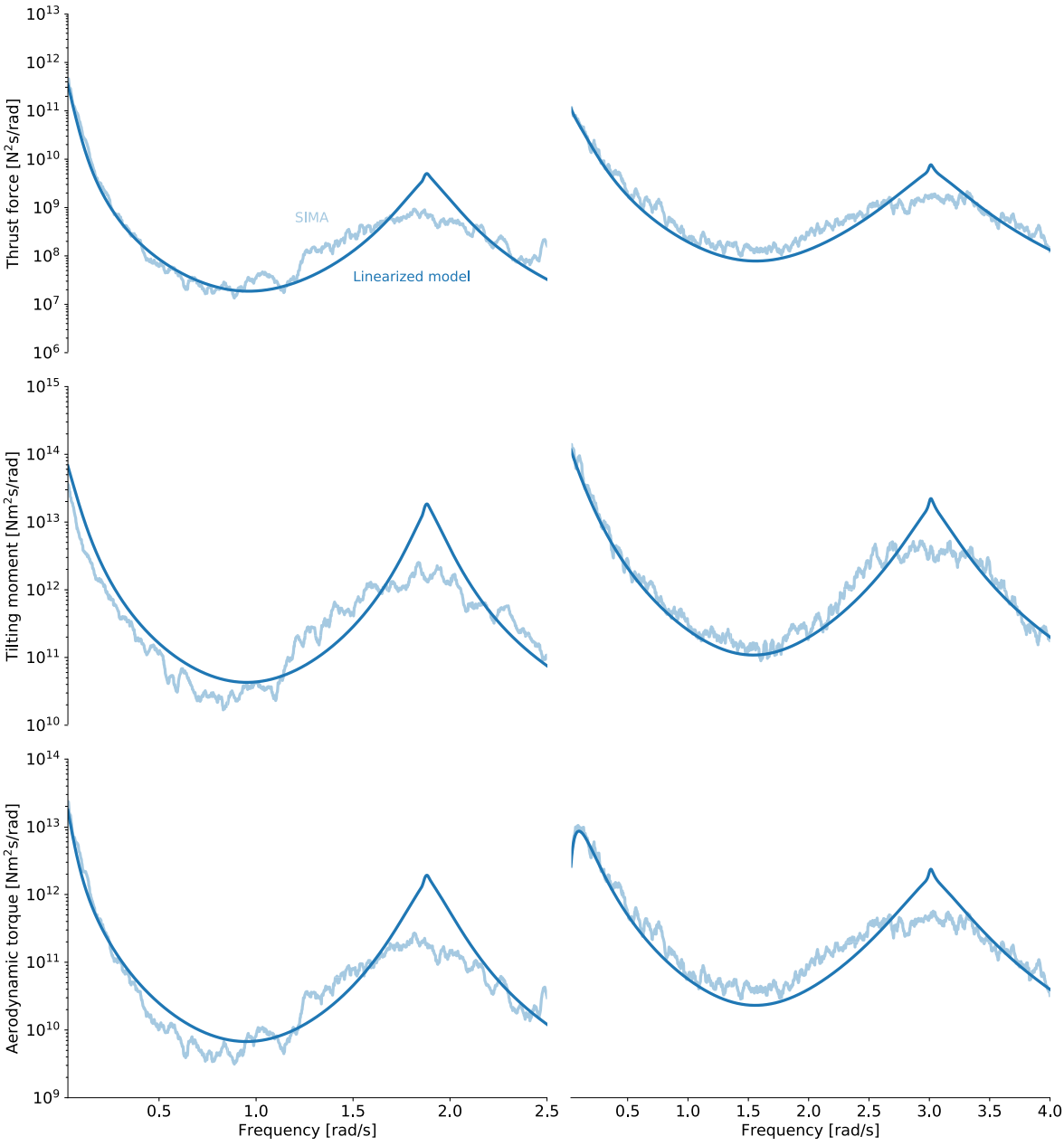

Fig. 4. Comparison of spectra for resultant aerodynamic loads on the tower top. Mean wind speeds of 7 m/s (left) and 15 m/s (right).

$$Q_{A,v} = 3\, M_{y,v}. \tag{39c}$$

The same relations hold for the derivatives with respect to the rotor speed and blade pitch angle; however, a change in rotor speed or collective blade pitch angle affects all parts of the rotor plane equally, and perturbations in these variables therefore do not contribute to the tilting moment. The total resultant aerodynamic forces are thus expressed as:

$$F_T \approx F_{T0} + F_{T,v}\Delta v + F_{T,\dot{\phi}}\Delta\dot{\phi} + F_{T,\theta}\Delta\theta, \tag{40a}$$

$$M_T \approx M_{T0} + M_{T,v}\Delta v, \tag{40b}$$

$$Q_A \approx Q_{A0} + Q_{A,v}\Delta v + Q_{A,\dot{\phi}}\Delta\dot{\phi} + Q_{A,\theta}\Delta\theta. \tag{40c}$$

2.5.4. Verification

To verify the linearized aerodynamic formulation, the resultant tower top loads are compared to results from nonlinear time-domain simulations performed using the SIMA software developed by SINTEF Ocean, which couples the RIFLEX [35] and SIMO [36] programs. Here, the blades are modelled using nonlinear beam elements, and the aerodynamic loads on the blades are computed using BEM theory with a Glauert correction, hub and tip loss factors, dynamic wake, dynamic stall, and tower shadow. The three-dimensional turbulent wind field is created using TurbSim [37], where the vertical wind shear is modelled by the power law with an exponent of 0.14 [38].

Fig. 4 shows the comparison for a fixed turbine with the control system active for mean wind speeds of 7 and 15 m/s. The results show overall good agreement, with the exception of frequencies close to the 3P frequency, where the linear model overestimates the loads. This discrepancy may be due to the assumption of constant rotor speed in the effective wind speed formulation, which causes the linear model to overestimate the response of the 1st bending mode (and thus the fatigue damage in the structure) if the natural frequency is close to the blade passing frequency. However, this is not expected to significantly affect the results from the optimization, because it is highly unlikely that the optimizer will converge to a design solution with the first bending frequency within the 3P range.

2.6. Environmental conditions

The fatigue design should consider all relevant environmental conditions (ECs) over the lifetime of the structure; however, to limit the computational effort, 30 ECs are used to evaluate the long-term fatigue performance in the present work. The mean wind speeds range from 1 to 30 m/s with 1 m/s steps. For each mean wind speed, the most probable values for the significant wave height and spectral peak period are used. These values, as well as the probability associated with each condition, are found from the joint probability distribution presented by Johannessen et al. [39], and shown in Fig. 5. The probabilities are normalized to achieve a total probability of unity, i.e.,

$$\sum_{i=1}^{N_{EC}} p_i = 1, \tag{41}$$

where N_{EC} is the number of ECs considered in the analysis, and p_i is the probability of condition i.

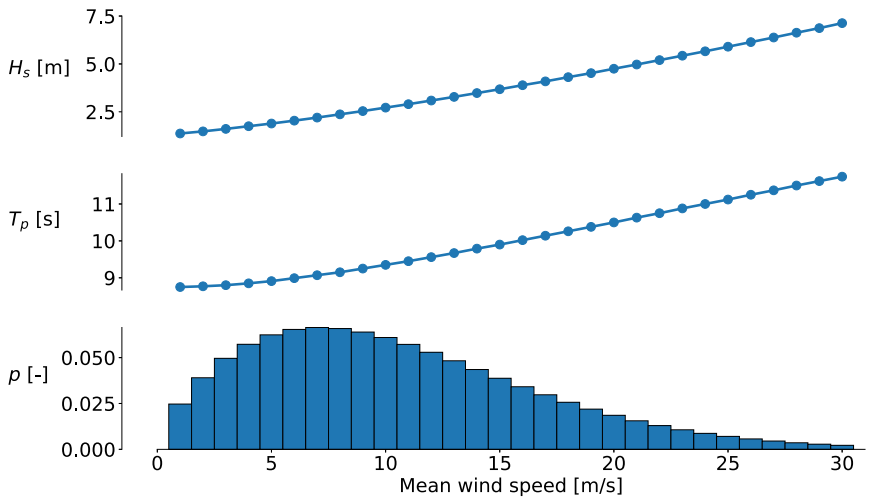

Fig. 5. Significant wave heights, spectral peak periods, and normalized probabilities associated with mean hub height wind speeds applied in the fatigue calculations.

The three ECs described in Table 1, which are located on the 50-year contour surface, are selected to evaluate the extreme response. In EC 1, the mean wind speed is close to the rated speed of the turbine, which yields the maximum thrust force on the rotor. EC 2 considers an operational condition with above-rated wind speed, while EC 3 represents a wind speed above cut-out, where the turbine is parked and the blades are feathered.

For all ECs, a Kaimal spectrum for IEC class B turbines and a normal turbulence model (NTM) [34] are used to describe the incoming wind.

3. Optimization problem

The present optimization study considers the design of four different subsystems simultaneously:

1. Spar platform
2. Wind turbine tower
3. Mooring system
4. Blade-pitch control system

The formulation of the optimization problem is described in the following subsections.

3.1. Framework

The FWT model is implemented in OpenMDAO [15], which is an open-source framework for multidisciplinary design, analysis and optimization. A modular approach is utilized, where smaller units of code (components) are connected to form the larger and more complex multidisciplinary model. Inputs, outputs, and partial derivatives for each component are given to the framework, which handles the data transfer between different parts of the code, performs the analysis, and calculates the total system derivatives needed by the optimizer [40]. To analyse a large number of load cases in an efficient manner, the code is parallelized using MPI.

The design is optimized using a gradient-based approach where analytic derivatives are computed for the coupled model. Analytic gradient computation requires significant implementation effort, but offers increased computational efficiency and accuracy compared to finite-difference approximations. The total derivatives are computed using the adjoint method, whose cost is independent of the number of design variables [41]. With the current model, which has 80 inputs and 18 outputs, the run time for the gradient computation is roughly 4× the analysis time, where a single wind-wave condition runs in approximately 5 s on a standard laptop. The model layout and data dependencies are illustrated using an extended design structure matrix (XDSM) [42] in Fig. B.1 in Appendix B.

The SNOPT algorithm [43] is used to solve the optimization problem. SNOPT uses a sequential quadratic programming (SQP) approach to solve nonlinear constrained optimization problems, and is connected to OpenMDAO using the pyOptSparse interface [44].

Because gradient-based methods have the problem of potentially getting stuck in local minima if the objective function is multi-modal, the optimization is run starting from several initial design points.

3.2. Objective

Ideally, a FWT design optimization procedure should try to minimize the levelized cost of energy (LCOE), which is the lifetime costs of the system divided by the total energy production. However, because the LCOE depends on numerous unknown parameters that cannot be included properly in an engineering optimization model, simpler objectives are needed. A common choice is the weight or the associated material costs of the system, but cost functions that do not take into account production cost components, such as welding, are considered unrealistic [10]. In addition, a measure of the power production performance should be included. The amount of produced energy will mostly depend on the wind farm site and is unlikely to vary much with the design of the FWT system. Another relevant performance measure is the quality of the power delivered by the turbine, which describes how much the energy output fluctuates. High-quality power, which has low variability in the output, is desirable, and its value for a given design is proportional to the variation in rotor speed. The objective function used in the present work is thus a weighted combination of two parameters: the system costs, C_{total}, which cover material and manufacturing, and the weighted average of the rotor speed standard deviation, $\sigma_{(\dot{\phi})}$, which is a measure of the power quality:

$$f = w_1 C_{\text{total}} + w_2 \sigma_{(\dot{\phi})}. \tag{42}$$

Table 1
Environmental conditions for extreme response calculations.

Condition	1	2	3
Mean wind speed at hub height, U (m/s)	11.0	21.0	50.0
Significant wave height, H_s (m)	7.5	9.9	15.1
Spectral peak period, T_p (s)	12.0	14.0	16.0
Turbulence intensity at hub height, I (−)	0.18	0.14	0.12

The relative importance is controlled by the weight factors w_1 and w_2, where $w_1 + w_2 = 1; w_1, w_2 \in [0, 1]$. Because the monetary cost of reduced power quality is difficult to quantify, the optimization is run with different values for the weight factors, to assess the trade-off between the two sub-objectives.

The total cost of the system is

$$C_{\text{total}} = C_{\text{spar}} + C_{\text{tower}} + C_{\text{moor}}, \tag{43}$$

where C_{spar}, C_{tower} and C_{moor} are the costs of the platform, tower, and mooring system, respectively. The platform and tower costs take into consideration both material and manufacturing, using cost models from Farkas and Jármai [45]. Costs related to installation, maintenance, and decommissioning are not included. The cost of the platform (and similarly for the tower) is expressed as

$$C_{\text{spar}} = k_m M_{\text{spar}} + k_f \sum_i T_i, \tag{44}$$

where k_m is the steel cost factor, M_{spar} is the steel mass of the hull, and k_f is the fabrication cost per unit time. T_i is the time spent at fabrication stage i, expressed as a function of the geometry. The manufacturing costs include forming of plate elements into shells, assembly, welding, and painting. The ratio between the material and fabrication cost factors, k_m/k_f, depends on the labour cost, which varies with the fabrication site. In the present work a ratio of 1.0 is assumed, which is a typical value for West European labour [45]. Based on numbers from Teillant et al. [46], the cost of structural steel is about 80 times the cost of concrete ballast (per kg). The cost of ballast is therefore neglected in the current work.

Many different estimates for the cost of steel for floating support structures can be found in the literature, spanning from 1.0 €/kg (only material [47]) to 4.5 €/kg (including manufacturing and assembly [14]). Here, the steel cost factor, k_m, is assumed to have a value of 2.7 €/kg, which is approximately the same as the value used by Fylling and Berthelsen [11]. The mooring line costs are expressed as a function of weight, with a price of 3–4.5 €/kg, depending on the grade [48]. In the present work, steel grade R4 with an associated cost of 3.5 €/kg is assumed, which results in mooring line costs that are about 5–10% of the support structure costs. The relative importance of mooring and support structure costs, which is somewhat uncertain, may affect the optimization results due to trade-off effects; however, preliminary analyses indicate that the system is fairly insensitive to the cost distribution.

The weighted average of the rotor speed standard deviation, used in Eq. (42), is computed by summing the values from each of the 30 FLS conditions described in Section 2.6, weighted by the probability of the condition:

$$\sigma_{(\dot{\phi})} = \sum_{i=1}^{N_{\text{EC}}} p_i \sigma_{(\dot{\phi}),i}, \tag{45}$$

where $\sigma_{(\dot{\phi}),i}$ is the rotor speed standard deviation for condition i.

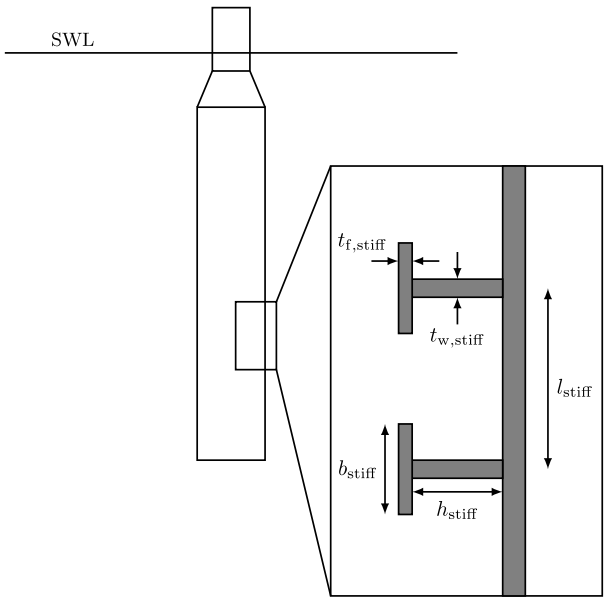

Fig. 6. Scantling design parameters.

3.3. Design variables

3.3.1. Spar platform

In the design process, the hull is discretized using ten sections in the vertical direction. The length of each section, as well as the diameter and wall thickness at each connecting node are included as design variables in the optimization. The diameter and wall thickness are assumed to vary linearly within each element. The number of elements that must be welded together during production is assumed to be equal to the number of hull sections, and is thus independent of the section lengths.

In addition, the study considers the scantling design of the hull. The spar platform is assumed to be equipped with circumferential T-ring stiffeners, which are described by five variables: the thickness and length of the web and flange, and the distance between the stiffeners. This is illustrated in Fig. 6. The ring stiffener variables are assumed to be constant within each section of the hull, and a material density of 7850 kg/m^3 is used for all components.

3.3.2. Tower

Similarly to the platform, the tower is parameterized as ten sections with linearly interpolated cross sectional properties. The section lengths are kept fixed during the optimization to achieve the same hub height as the original DTU 10 MW turbine at 119 m above SWL. Here, each section has a length of 10.5 m, except for the uppermost section, which has a length of 11.13 m. The design variables are the diameter and wall thickness for each section, and the inner structure in the tower is not considered. Because secondary structures in the tower are not modelled, the material density is increased to 8500 kg/m^3 to achieve a more realistic tower mass [19].

3.3.3. Mooring system

The mooring system optimization includes four design variables: the mooring line diameter, the depth of the fairleads below the SWL, the total length of the lines, and the horizontal distance between fairlead and anchor. Because the analyses only consider the 2D response of the turbine with co-directional wind and waves, the layout of the mooring system in the horizontal plane is not considered in the study.

The mooring line diameter affects both the mass and stiffness properties of the lines. The equations for the submerged weight and axial stiffness, w_{moor} and EA_{moor} respectively, are taken from Barltrop [49]:

$$w_{\text{moor}} = 0.1875\, D_{\text{moor}}^2 \quad [\text{N}/\text{m}] \tag{46}$$

and

$$EA_{\text{moor}} = 90000\, D_{\text{moor}}^2 \quad [\text{N}], \tag{47}$$

where D_{moor} is expressed in mm.

Table 2
Design variables used in the study.

Description	Symbol	Number of variables	Units
Spar diameter	D_{spar}	11	m
Spar wall thickness	t_{spar}	11	m
Spar length	L_{spar}	10	m
Ring stiffener flange thickness	$t_{\text{f,stiff}}$	4	m
Ring stiffener web thickness	$t_{\text{w,stiff}}$	4	m
Ring stiffener flange width	b_{stiff}	4	m
Ring stiffener web height	h_{stiff}	4	m
Ring stiffener distance	l_{stiff}	4	m
Tower diameter	D_{tower}	11	m
Tower wall thickness	t_{tower}	11	m
Mooring line diameter	D_{moor}	1	m
Fairlead depth	z_{moor}	1	m
Mooring line length	L_{moor}	1	m
Horizontal distance from fairlead to anchor	x_{moor}	1	m
Proportional gain of blade-pitch controller	k_p	1	rad·s/rad
Integral gain of blade-pitch controller	k_i	1	rad/rad

3.3.4. Control system

The control system optimization considers the proportional and integral gains of the blade-pitch PI controller. Although more advanced control strategies are not employed in the present work, they could be implemented with their associated parameters as design variables within the present framework, as long as the system can be reasonably accurately represented by a linear control model. A relevant example is the well-known "negative damping problem" related to the blade-pitch controller above rated wind speed, which can induce instabilities in the platform motions of the system [50]. A suggested way to resolve this issue is to use a feedback term proportional to the nacelle velocity [51] or platform pitch velocity [52] to manipulate the rotor speed set point. The velocity feedback gain could then be incorporated as a design variable in the optimization process.

3.3.5. Summary

Concatenating the design variables for each of the subsystems described in the previous sections would result in a total of 110 design variables. To reduce the required computational effort, the number of design variables is decreased by introducing B-splines for the ring stiffener parameters. B-splines use a pre-defined number of control points, which we set to $n_{cp} = 4$, to produce smooth distributions for the parameters. The remaining support structure design variable vectors are kept at their original sizes, because we found this to result in better optimization convergence. Thus, the optimization problem was reduced to the 80 design variables detailed in Table 2.

3.4. Constraints

The present optimization study includes constraints related both to fatigue (FLS) and ultimate (ULS) limit states for the system. In addition, a number of restrictions are added to avoid non-physical or infeasible design solutions, as detailed below. These may not be stated explicitly in design standards, but are chosen here based on common practice or engineering judgment.

3.4.1. Spar platform

The fatigue damage in the hull is calculated at each node using SN curves and the Dirlik method. The D curve with cathodic protection developed by DNV GL [53] is applied together with a design fatigue factor (DFF) of 3.0. This DFF is higher than the minimum required value given by DNV GL [54], but corresponds to the DFF for a normal safety class in the previous DNV standard [55]. The lifetime of the FWT system is chosen to be 20 years, and the fatigue design constraint that needs to be satisfied is thus expressed as

$$D_{\text{tot}} \leq \frac{1.0}{\text{DFF}}, \tag{48}$$

where D_{tot} is the total fatigue damage in 20 years:

$$D_{\text{tot}} = N_{20} \sum_{i=1}^{N_{\text{EC}}} p_i D_i. \tag{49}$$

Here, N_{20} is the number of short term conditions in 20 years, and D_i is the fatigue damage in condition i.
Hull buckling is assessed using design criteria stated by DNV GL [56], where the following buckling modes are considered:

1. Shell buckling: Buckling of shell plating between ring stiffeners
2. Panel ring buckling: Buckling of shell plating including ring stiffeners
3. Column buckling: Buckling of the cylinder as a column

For shells, the stability requirement is given by

$$\sigma_{j,\text{Sd}} \leq f_{\text{ksd}}, \tag{50}$$

where $\sigma_{j,\text{Sd}}$ is the design equivalent von Mises stress, and f_{ksd} is the design shell buckling strength. To avoid panel ring buckling, several requirements must be met. The cross sectional area of the ring frame, A_{stiff}, must satisfy

$$A_{\text{stiff}} \geq \left(\frac{2}{Z_l^2} + 0.06\right) l_{\text{stiff}}\, t_{\text{spar}}, \tag{51}$$

where Z_l is a curvature parameter. Also, the effective moment of inertia of the ring frame, I_{stiff}, must satisfy

$$I_{\text{stiff}} \geq I_x + I_{xh} + I_h, \tag{52}$$

where the terms on the right hand side are the minimum required moments of inertia for cylindrical shells subjected to axial, bending, or both (I_x), torsion, shear, or both (I_{xh}), and external hydrostatic pressure (I_h). Because the ballast inside the platform is assumed to be solid, the horizontal pressure from the ballast, which counteracts the external pressure, is not accounted for in the buckling calculations [54]. To avoid local buckling of the ring frame, the web height is limited to

$$h_{\text{stiff}} \leq 1.35\, t_{\text{w,stiff}} \sqrt{\frac{E}{f_y}}. \tag{53}$$

The torsional buckling of the ring frame need not be considered if

$$b_{\text{stiff}} \geq \frac{7 h_{\text{stiff}}}{\sqrt{10 + \frac{E}{f_y}\frac{h_{\text{stiff}}}{r}}}, \tag{54}$$

where E is the Young's modulus, and r is the mid-plane shell radius. The yield stress, f_y, is set to 355 MPa. To avoid assessing column buckling, the following equation should be satisfied

$$\left(\frac{kL_C}{i_C}\right)^2 \leq 2.5\frac{E}{f_y}, \tag{55}$$

where k is the effective length factor (set to 1.0), L_C is the total length of the cylinder, and i_C is the radius of gyration for the cylinder section. For the hull buckling, a load factor $\gamma_F = 1.35$ is applied on the environmental loads [54], while the material factor, γ_M, is given by the following equation [54]:

$$\gamma_M = \begin{cases} 1.10, & \bar{\lambda}_s < 0.5 \\ 0.80 + 0.60\,\bar{\lambda}_s, & 0.5 \leq \bar{\lambda}_s \leq 1.0 \\ 1.40, & \bar{\lambda}_s > 1.0, \end{cases} \tag{56}$$

where $\bar{\lambda}_s$ is the reduced shell slenderness defined in DNV GL [56].

The buoyancy forces should be equal to the total weight of the system, which is achieved by filling the inside of the platform with concrete ballast from the bottom until equilibrium is reached. In addition, the platform is limited to have a maximum pitch angle of no more than 15° in any of the extreme ECs. A maximum offset requirement of 32 m, which corresponds to 10% of the water depth, is also applied to avoid breakage of the power cable. These constraints are based on common industry practice and should be verified before they are used in an actual design process.

Another potentially constrained response parameter is the nacelle acceleration, which has been frequently considered in design optimization of FWTs, either as a constraint [11,57] or as part of the objective function [7,8]. The rationale behind setting a limit on the maximum acceleration at the nacelle is typically related to reduced loads on the drivetrain; however, a recent study by Nejad et al. [58] found that the accelerations at the tower top were not a good indicator for either maximum or fatigue loads on the main bearings of the gearbox. This parameter is therefore not considered in the present work.

The heave response is not calculated in the model and is therefore not constrained, but the natural period in heave is limited to minimum 25 s to avoid the possibility of heave resonance in the wave frequency range. Here, the added mass in heave is approximated as the value for a 3D circular disc provided by DNV GL [59], with the same diameter as the bottom of the platform.

Another issue relevant for spar platforms is the phenomenon known as Mathieu instability, which can occur when the pitch restoring moment varies harmonically due to large heave motions [60]. Haslum and Faltinsen [61] reported that unstable solutions occur when the ratio between the heave motion and the pitch natural frequency is 0.5, 1.0, 1.5, or 2.0. Mathieu instability is avoided in the current work by placing a constraint on the ratio between the natural periods in heave and pitch, to prevent it from reaching a value close to one of the critical ratios.

The presented model is only strictly valid for hull sections with vertical walls. However, the diameter varies with the platform nodes, and abrupt changes in geometry are unwanted due to fatigue performance. Therefore, the sections are conical in reality. To avoid platform shapes where the physics are not captured correctly by the model, a maximum taper angle of 10° is applied as a constraint for each section.

To limit the computational effort, constraints that must be satisfied along the length of the platform, such as the fatigue and buckling constraints, are aggregated using Kreisselmeier–Steinhauser (KS) functions [62,63]. This is also done for constraints that must be satisfied in each of the 50-year conditions.

3.4.2. Tower

The fatigue damage in the tower is assessed in the same way as described for the platform, but with the D curve in air and DFF = 2.0 [55].

Tower buckling is assessed using Eurocode 3 [64], assuming that the tower is stiffened between each section to reduce the buckling length. For each tower section, the following equation must be satisfied

$$\sigma_x \leq \frac{\sigma_{cr}}{\gamma_M \gamma_F}, \tag{57}$$

where σ_x is the axial stress on the outer radius of the tower, σ_{cr} is the critical buckling stress, and γ_F and γ_M are load and material factors, respectively. The factors applied in the current work are $\gamma_M = 1.1$ [65] and $\gamma_F = 1.35$ [54]. To ensure a smooth transition between the platform and tower, the tower base diameter and wall thickness are set equal to the diameter and wall thickness at the platform top. As for the hull, KS functions are used to aggregate the constraints.

3.4.3. Mooring system

Two constraints are applied to the mooring system: the maximum mooring line tension should not exceed the breaking strength of the chain, and the tension at the anchor should be purely horizontal. The first constraint is expressed as [54]

$$T_d \leq 0.95\, S_{\text{mbs}}, \tag{58}$$

where S_{mbs} is the minimum breaking strength and T_d is the design tension,

$$T_d = \gamma_{\text{mean}}\, T_{c,\text{mean}} + \gamma_{\text{dyn}}\, T_{c,\text{dyn}}. \tag{59}$$

Here, $T_{c,\text{mean}}$ and $T_{c,\text{dyn}}$ are the characteristic mean tension and the characteristic dynamic tension in the 50-year condition, respectively, and $\gamma_{\text{mean}} = 1.3$ and $\gamma_{\text{dyn}} = 1.75$ are the load factors for the normal safety class [54]. The minimum breaking strength is computed using

$$S_{\text{mbs}} = c\, D_{\text{moor}}^2 (44 - 0.08 D_{\text{moor}}), \tag{60}$$

where c is a constant dependent on the mooring chain grade [66].

The second constraint is based on the assumption that the anchors are not designed to take vertical forces, which requires the mooring lines to have sufficient length to avoid uplift at the anchors in all relevant ULS conditions [67]. The constraint limits the maximum experienced offset at the fairleads to be less than the critical value, which is found from an iteration scheme where the offset is increased until the effective length of the mooring line equals the total line length.

3.4.4. Control system

For certain combinations of the PI controller gains, the FWT system may become unstable. This is avoided by adding a requirement that the closed-loop poles of the system should have negative real parts, which ensures stability [68]. Analyzing the poles of the linearized system is not an exact method for determination of stability; Sandner et al. [69] found that a spar FWT with gains that gave poles in the right half plane still showed reasonable performance in nonlinear simulations. However, this analysis provides a starting point for a more detailed design of the control system.

4. Results

The results of the optimization study, presented in the following subsections, are divided into six parts. First, we discuss the multimodality of the design space, and identify local minima. Trade-off effects between the two sub-objectives in Eq. (42) are then assessed by running the optimization problem stated in Section 3 with different weight factors. Subsequently, a single combination of weight factors is selected, and the resulting optimized design of the support structure, mooring system, and controller is described in detail. Finally, the design is verified using nonlinear time domain simulations.

4.1. Soft-stiff and stiff-stiff tower design

The fatigue damage in the support structure increases significantly if the natural frequency of the first tower bending mode coincides with the blade passing frequency, and the optimizer will therefore try to move the tower mode away from the 3P range. The direction that the mode is moved during the optimization will depend on the initial design, as illustrated in Fig. 7. Due to the "barrier" created by the blade passing frequency, the optimizer will not be able to move over to the stiff-stiff range if the initial design has a soft-stiff tower, and vice versa.

Initial studies performed in this work showed that the tower mode had to be placed in the stiff-stiff range for the optimization problem to converge to a feasible solution, because the optimizer was unable to find a design that satisfied the fatigue constraints in the

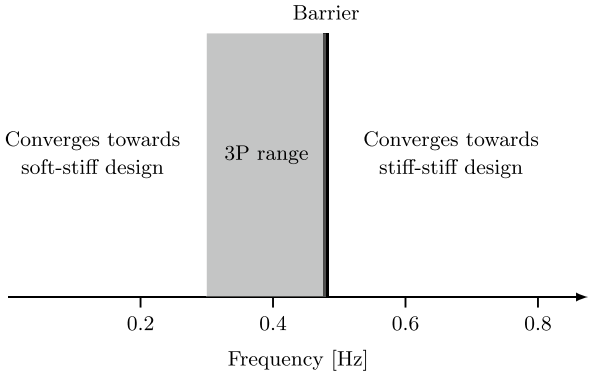

Fig. 7. Impact of initial tower bending natural frequency on optimization results.

soft-stiff range. Although these results suggest that it is challenging to design such a FWT system with a soft-stiff tower, it should not be treated as proof that a solution does not exist. The design analyses are based on a simplified model and a reduced set of ECs for the long-term fatigue calculations, which may give inaccurate results for certain combinations of parameters. In addition, more advanced control strategies, such as a speed exclusion zone to prevent tower resonance in the below-rated regime, could improve the fatigue behaviour. More detailed studies of potential designs are therefore needed to conclude whether a feasible soft-stiff tower design is possible.

4.2. Trade-offs between system costs and power quality

To assess the trade-offs between costs and power quality for the system, the optimization is performed with different values for the weight factors in Eq. (42). Here, the rotor speed standard deviation is normalized by the value achieved with the land-based DTU 10 MW wind turbine and the original controller [70], found from nonlinear time domain analyses using SIMA. The land-based weighted average rotor speed standard deviation is found to be 0.043 rad/s. Because the present work considers a floating system with a simplified controller, the rotor speed variations are expected to be larger than the land-based reference value.

The results, shown in Fig. 8, suggest that a significant reduction in rotor speed variation can be achieved with relatively small increases in the total costs. However, these results are dependent on the environmental conditions that drives the extreme response. The reduction in rotor speed variation is primarily achieved by modifying the blade-pitch controller gains, but for both platform motions and buckling loads in the support structure, the below-rated 50-year condition (EC 1) yields the largest response. Therefore, the blade-pitch controller does not affect the extreme response of the system, and the trade-off effects are limited to the response in the above-rated fatigue conditions, where a faster controller (and thus better rotor speed tracking) leads to an increase in the fatigue loads and consequently to an increase in material costs.

In the following sections, the results are presented for the case shown with a black circle in Fig. 8, which corresponds to $w_1 = 7\times 10^{-8}$ and $w_2 = (1 - 7\times 10^{-8})$ in Eq. (42).

4.3. Platform and tower

The optimized tower and platform design, including fatigue and buckling utilization, is shown in Fig. 9. For the hull, the value for the most critical buckling mode is shown.

The probable reason for the relatively small platform diameter in the wave zone is to reduce the wave loads on the structure. Because a smaller diameter increases the axial stress for a given bending moment, and because the fatigue loads in this part of the structure are large, a large wall thickness is needed in this area to satisfy the FLS design criteria. Fatigue is the critical failure mode down to a depth of approximately 10 m, beyond which buckling due to hydrostatic pressure becomes the constraint driving the design.

Below the wave zone, the hull exhibits an hourglass shape, with maximum and minimum values for the diameter approximately 32 m and 56 m below the SWL, respectively. The sharp edges located where the diameter reaches its maximum and minimum and the constant gradient between them is a result of the maximum taper angle constraint being active for most of the platform sections. The constraint is a consequence of the simplified hydrodynamic and structural formulations, and its value is based solely on engineering judgment. The results indicate that the performance of the platform can be further improved if this constraint is relaxed, which might require a more comprehensive numerical model and possibly more information about the effect of the platform shape on the manufacturing costs.

The hourglass shape serves several purposes that are beneficial for the platform dynamics. The large diameter just below the wave

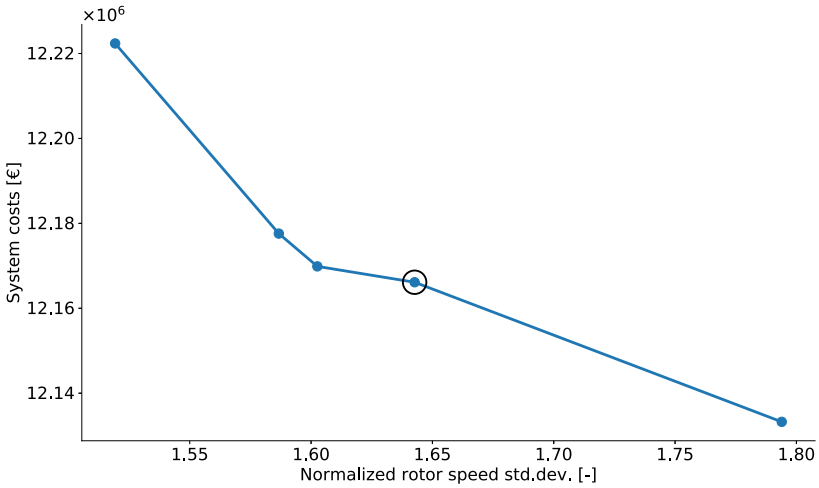

Fig. 8. Trade-offs between rotor speed variation and system costs in the multiobjective optimization.

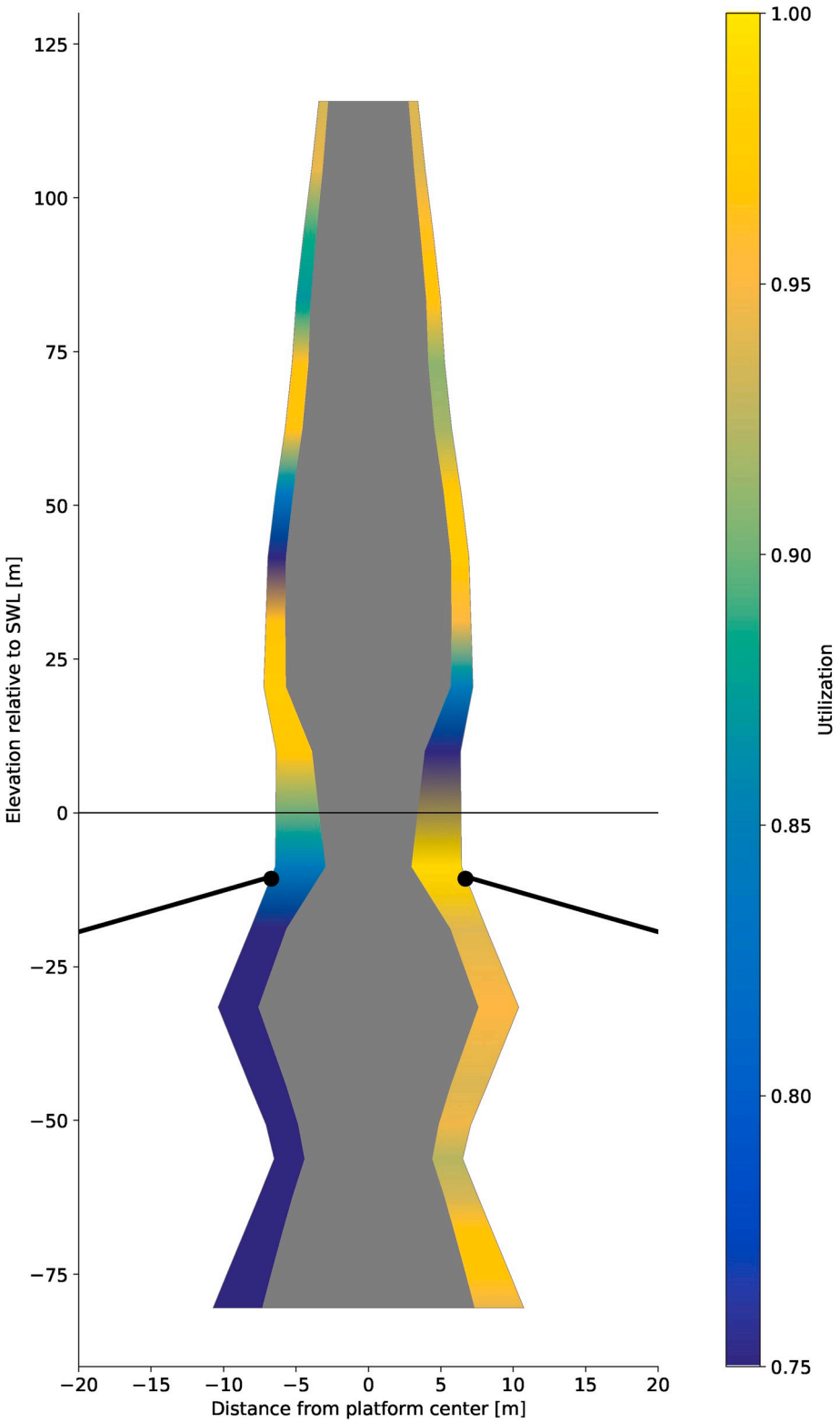

Fig. 9. Optimized tower and platform design with fatigue utilization (left) and buckling utilization (right). The wall thickness is scaled by a factor of 40 relative to the diameter for visualization purposes.

zone raises the centre of buoyancy (CoB), and because spar platforms achieve most of their restoring moment in roll and pitch from the distance between the CoB and the total centre of gravity (CoG), this effectively increases the rotational stiffness of the system.

The increase in diameter near the bottom of the spar can be explained by two factors. First, because the hull is filled with concrete ballast from the bottom until equilibrium between weight and buoyancy is reached, a consequence of the increased diameter is that a larger share of the required ballast can be placed near the bottom, which lowers the platform CoG. Second, the increased surface area at the bottom increases the added mass and thus the natural period in heave, which is constrained from below to avoid resonance in the wave-frequency range. One effect of increasing the restoring moment is that the natural period in pitch is reduced. At higher frequencies, there is less energy in the wind (less turbulence) and thus less excitation around the natural frequency as well.

The lower draft compared to other designs, such as the 5 MW OC3-Hywind design [71], is advantageous from a material cost point of view, because the high hydrostatic pressure at large depths requires thick-walled sections. Although costs related to installation are not a part of the objective in the current optimization scheme, a shallower draft is also favourable with respect to assembly and towing to site, which is one of the challenges related to spar buoys.

Both the maximum platform pitch constraint of 15° and the maximum offset constraint of 32 m in the 50-year conditions are active for the optimized design. The critical condition for both constraints is EC 1, where the mean wind speed is close to rated. The static pitch angle at rated thrust for the optimized design is 7.7°. The key characteristics for the optimized spar platform are listed in Table 3, while natural periods for the system in calm air are listed in Table 4. Distributed properties for the optimized platform and tower are given in Tables 10 and 11 in Appendix A.

Surprisingly, the diameter of the tower increases from the base and reaches its maximum at a height of 20.5 m above the SWL. This is uncommon for wind turbine towers, which typically are widest at the bottom and taper gradually towards the nacelle. The reason for this unconventional design is related to the integrated optimization approach, which takes into account the cost and performance of the tower and platform simultaneously. In general, within the limits set by the buckling constraints, the most cost-effective way to achieve the required fatigue performance for a given tower section is to increase the diameter and decrease the wall thickness. However, at the tower base, the diameter also has to match the diameter at the top of the platform, which should be reduced to limit the wave loads on the structure. The result of these conflicting influences is that the optimized tower starts with a smaller-than-optimal diameter at the base and consequently larger-than-optimal wall thickness (from the point of view of an isolated tower), before the diameter is increased and the wall thickness is significantly reduced.

The spar platform has clearly separated areas where the design is driven by either fatigue or ultimate loads because of the large bending moments in the wave zone and high hydrostatic pressure in the lower parts. Unlike the spar platform, both tower constraints are dominated by bending moments. Consequently, the optimizer is able to find a tower design where both the FLS and ULS constraints are close to the limit along the whole length. Table 5 lists the main parameters of the optimized tower, where the elevations to the tower base and tower top are fixed during the optimization.

In Fig. 10, the optimized tower design is compared to the tower of the OO-Star Wind Floater Semi 10 MW, which was part of the LIFES50+ project [72]. The comparison shows that the present design in general has a larger diameter and a smaller wall thickness than the OO-Star tower. Comparing the overall tower properties, the mass of the tower optimized in the present work is approximately 24% lower than the OO-Star tower, despite using a slightly larger effective mass density (8500 vs. 8243 kg/m^3). The natural frequency of the first fore-aft tower bending mode (with flexible substructure) is 0.8 Hz and 0.59 Hz for the optimized tower and the OO-Star tower, respectively, which places them both well within the stiff-stiff range. One drawback with the large diameter in the tower presented here is that tower shadow effects, which are not considered in the model, become more prominent. This may in turn lead to increased loads on the blades and increased 3P excitation on the tower, which could complicate the design process.

The optimized scantling design parameters are shown in Fig. 11. All five variables follow the same pattern, where a reduced distance between stiffeners results in smaller required stiffener size. In general, the most critical buckling mode driving the ring stiffener design is the buckling of the shell plating.

4.4. Control system

The optimized control system parameters for different weight factors are plotted against the resulting power quality in Fig. 12. Increasing the gains results in a faster controller, leading to lower variation in the rotor speed.

To assess the importance of integrating the controller in the FWT design loop, the optimization procedure is repeated with the control parameters k_p and k_i fixed at their initial values, as shown in Table 6. The values are those obtained by Hegseth and Bachynski [20], where a simple detuning procedure was used to reduce the bandwidth of the original DTU 10 MW controller [70] and thus place

Table 3
Optimized platform properties (without tower and turbine).

Parameter	Value	Units
Draft	80.4	m
Mass including ballast	1.57×10^7	kg
Displacement	1.72×10^4	m^3
Moment of inertia about CoG	4.66×10^9	kgm^2
Vertical CoG below SWL	66.0	m
Vertical CoB below SWL	42.9	m

Table 4
Natural periods for the optimized FWT system.

Mode	Value	Units
Surge	144.7	s
Pitch	34.4	s
Heave	25.0	s
1st bending	1.25	s

Table 5
Optimized tower properties.

Parameter	Value	Units
Elevation to tower base above SWL	10.0	m
Elevation to tower top above SWL	115.63	m
Total mass	9.5×10^5	kg
Vertical CoG above SWL	49.1	m
Moment of inertia about CoG	7.46×10^8	kgm^2

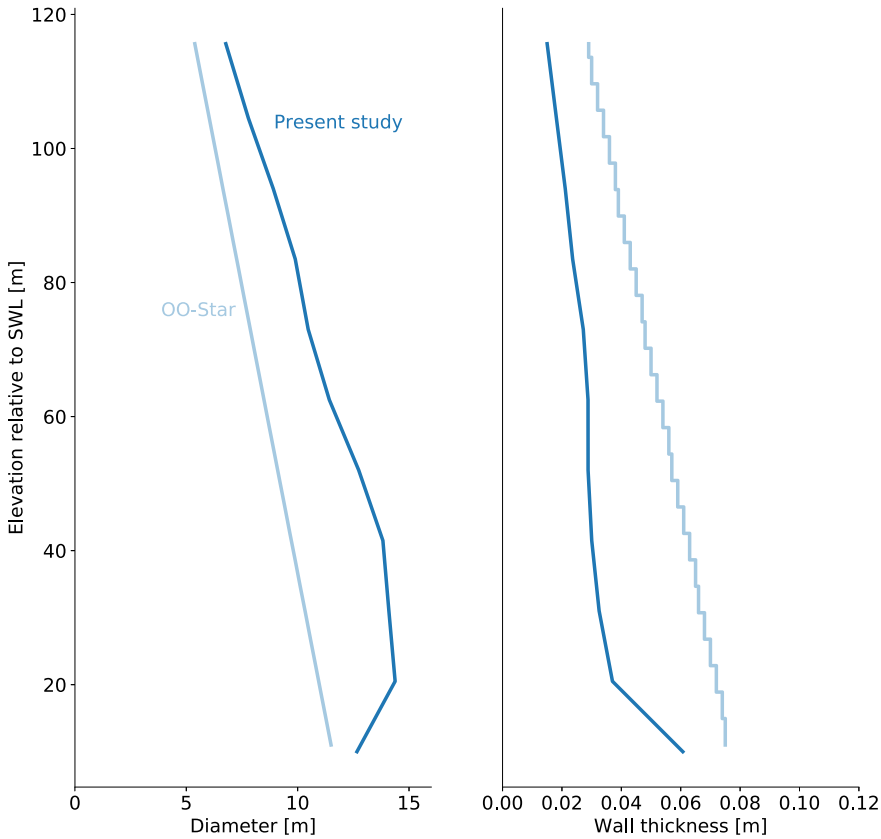

Fig. 10. Comparison of optimized tower design with LIFES50+ OO-Star Wind Floater.

it below the platform pitch natural frequency, while the damping ratio was kept constant.

The cost and power quality for the optimized solutions with and without the controller (for the same objective function weights) are shown in Table 7. Using the initial detuned controller results in both slightly higher costs, due to larger fatigue loads in the tower, and larger rotor speed variation. Although the actual numbers depend on the values used for the gains and thus are only valid for this particular example, it shows that neglecting the controller in the structural design process may lead to more expensive solutions with lesser performance.

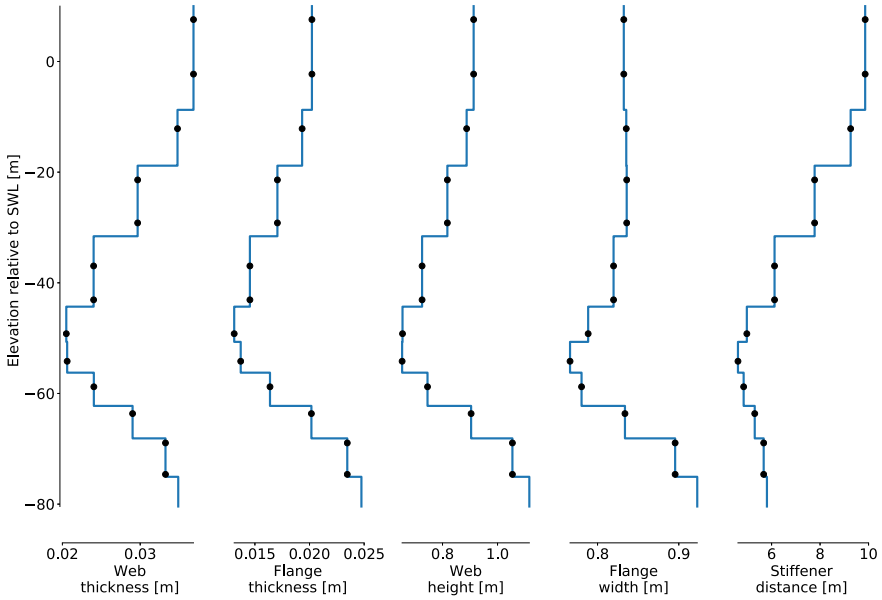

Fig. 11. Optimized ring stiffener parameters. The black dots show a possible stiffener layout.

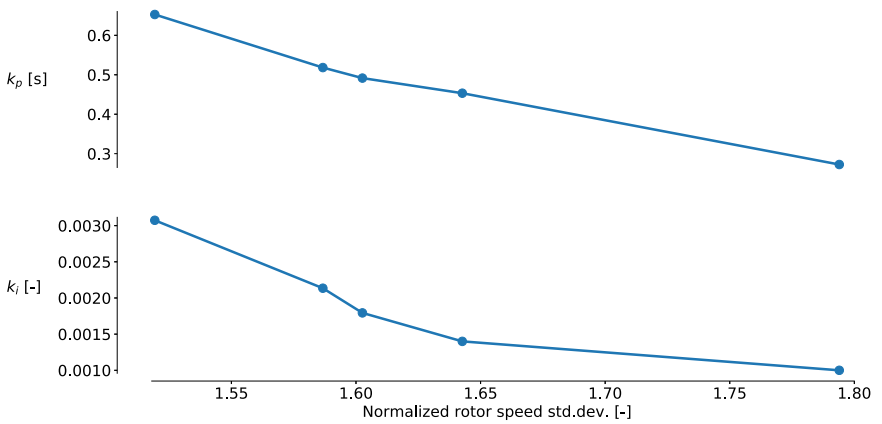

Fig. 12. Optimized blade-pitch controller gains plotted against resulting rotor speed variation.

Table 6
Fixed control system parameters.

Parameter	Value	Units
k_p	0.1794	rad·s/rad
k_i	0.0165	rad/rad

Table 7
Objective function values with and without controller included in the optimization.

	System cost [10_6 €]	Normalized rotor speed std.dev. [−]
With controller	12.17	1.65
Without controller	12.19	1.82
Difference	0.2%	10.9%

4.5. Mooring system

The optimized mooring system parameters are listed in Table 8. The most critical ULS condition for both mooring system constraints is found to be EC 1, as for the maximum offset and pitch angle constraints in Section 4.3. This is due to the large thrust forces in this condition. The optimized solution consists of relatively long mooring lines to meet the requirement of no uplift at the anchors. The line length and thus the material costs of the system, could be significantly reduced if vertically loaded anchors were used; however, these types of anchors are more expensive to install [73]. More information about the total costs of the mooring system, including installation and anchoring, would be needed to identify the most cost-effective solution.

Based on the results presented here, the significance of designing the mooring system simultaneously with the platform is not as clear as for the tower or control system. Although the mass of the platform and tower affect the natural period in surge and subsequently the level of excitation around resonance, the surge response is mostly governed by the rotor and mooring system design and is to a large degree independent from the design of the support structure. The most important coupling effects between the support structure and mooring system are related to the location of the fairleads, which influences the surge-pitch coupling and thus the pitch response of the platform. The fairlead position also affects the fatigue damage in the hull because the mooring forces contribute to the internal loads in the platform. Another coupling effect is that low-frequency mooring line dynamics, which is dependent on the platform motions, will induce damping for the low-frequency platform response [74]. However, this coupling effect is not considered in the present work.

The delta connections are omitted from the mooring system in the present model, and the yaw response of the platform is neglected in the analysis. Since one of the main tasks of the mooring system for a spar FWT is to limit yaw motions [75], the optimized mooring design presented here may have to be modified to obtain satisfactory performance for the platform response. In addition, common mooring line components that can improve the system behaviour, such as buoys or clump weights, can not be modelled with the current methodology and are not considered.

4.6. Design verification

The proposed design optimization approach is verified by analysing initial and optimized designs using nonlinear aero-hydro-servo-elastic time-domain simulations in SIMA. Here, the tower, hull, and blades are modelled using nonlinear beam elements. Hydrodynamic loads in the horizontal direction are applied on the platform using MacCamy–Fuchs theory, together with viscous forces from the drag term in Morison's equation. In heave, the hydrodynamic loads are limited to buoyancy forces integrated up to the instantaneous free surface and added mass on the lower end of the platform, meaning that Froude–Krylov and diffraction forces are neglected. Since the heave response is not considered in the linearized model, and the first order wave excitation in heave is small, this is deemed acceptable for the present work.

Bar elements with only axial stiffness are used to model the mooring lines, and hydrodynamic loads on the lines are computed using Morison's equation. A rotational spring is added to the model to ensure that the yaw stiffness from the mooring system is included, using a spring stiffness of 1.48×10^8 Nm/rad. The aerodynamic loads on the rotor are computed using BEM theory as described in Section 2.5.4, and viscous drag forces on the tower are included.

The fatigue performance of the tower and hull is assessed by analysing the 30 FLS conditions using six 1-h realizations. Rainflow counting and the Miner–Palmgren rule are used to estimate the fatigue damage, which is taken as the average value over the six seeds. The extreme response, i.e., the most probable maximum value in 1 h in the 50-year conditions, is found using the AUR method, where the function describing the upcrossing rate is fitted to the empirical data [76]. 1-h simulations with 20 different random seeds are used for each 50-year condition.

The initial design is based on the "Spar 1" design obtained by Hegseth and Bachynski [20], but with 60% increase in wall thickness and 40% increase in diameter along the hull and tower to place the first tower mode in the stiff-stiff range. This FWT system has not been through a proper design process and does not represent a realistic solution. The purpose of including it in the verification is not to use it as a benchmark for the optimized design, but rather to show that the presented methodology is able to capture real trends.

Fatigue and buckling utilization factors from the nonlinear time-domain analyses are shown in Fig. 13 and Fig. 14 for the initial and optimal designs, respectively. For the initial design, the fatigue damage values are overestimated by the linear model in the wave zone and lower parts of the tower, where the largest utilization factors are found. This is primarily due to limitations in the Dirlik calculations in the current work, which assumes a single-slope SN curve valid for high-cycle fatigue. Therefore, this assumption becomes less accurate for designs with large damage values, where there is also a significant contribution from low-cycle fatigue. The buckling utilization factors agree very well, suggesting that the extreme response in this condition is relatively linear.

For the optimized designs, the fatigue damage and buckling utilization factors in the tower agree reasonably well with the results from the linearized model, which is usually conservative. This is primarily due to the overestimation of the platform pitch response in the linear model, which become more prominent in extreme conditions. Because the pitch response for the initial design is in general much smaller than for the optimized solution and thus contributes less to the bending moments in the structure, this effect is not seen for the initial design results in Fig. 13.

There is a notable difference between the linear and nonlinear models for the fatigue damage at the tower top in Fig. 14, where the accumulated damage based on time-domain simulations in SIMA is about twice as high. We believe this to be a consequence of somewhat non-Gaussian bending moment response at the tower top, which causes the accuracy of the Dirlik method to deteriorate. For the rest of the tower, the response is close to Gaussian, which earlier has been shown to result in good agreement between the Dirlik method and rainflow counting for spar FWTs [20].

Table 8
Optimized mooring system parameters.

Parameter	Value	Units
D_{moor}	0.081	m
z_{moor}	− 10.7	m
L_{moor}	1433.0	m
x_{moor}	1497.2	m

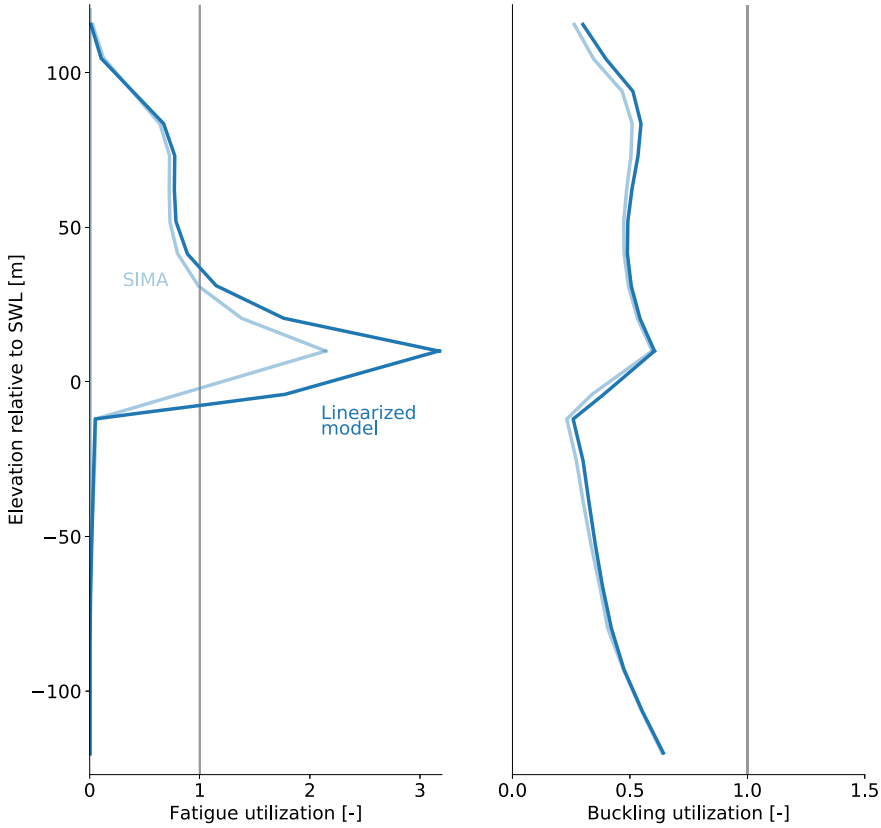

Fig. 13. Comparison of fatigue and buckling utilization factors, initial design.

Almost perfect agreement is observed for the hull buckling, despite the overprediction of the bending moments by the linear model. The reason for this is that the hydrostatic pressure, which is easily obtained without error, is the most important load component for buckling of the shell plating in the hull.

The extreme values for the offset, pitch angle, and mooring tension are listed in Table 9. The linearized model overestimates the platform motions, mainly because the aerodynamic loads are linearized and the mooring line damping is neglected. The mooring tension, on the other hand, is underestimated by the linear model, which also predicts a 4% decrease in the extreme value from initial to optimized design that is not observed in the nonlinear model.

5. Conclusions

A linearized aero-hydro-servo-elastic FWT model has been developed and used to optimize the design of the platform, tower, mooring system, and blade-pitch controller for a 10 MW spar FWT. The goal of the optimization is to minimize a weighted combination of the system costs and rotor speed variation, which is used as a measure of the power quality.

The results of the optimization depend on the initial tower design because a local minimum exist in both the soft-stiff and stiff-stiff range for the first bending mode. Initial analyses suggest that feasible soft-stiff tower designs may be challenging to achieve for these types of FWT systems, since no solution that satisfied the FLS constraints was identified by the optimizer. However, including more advanced control strategies could improve the fatigue behaviour in the soft-stiff range, and potentially result in a different global minimum for the problem.

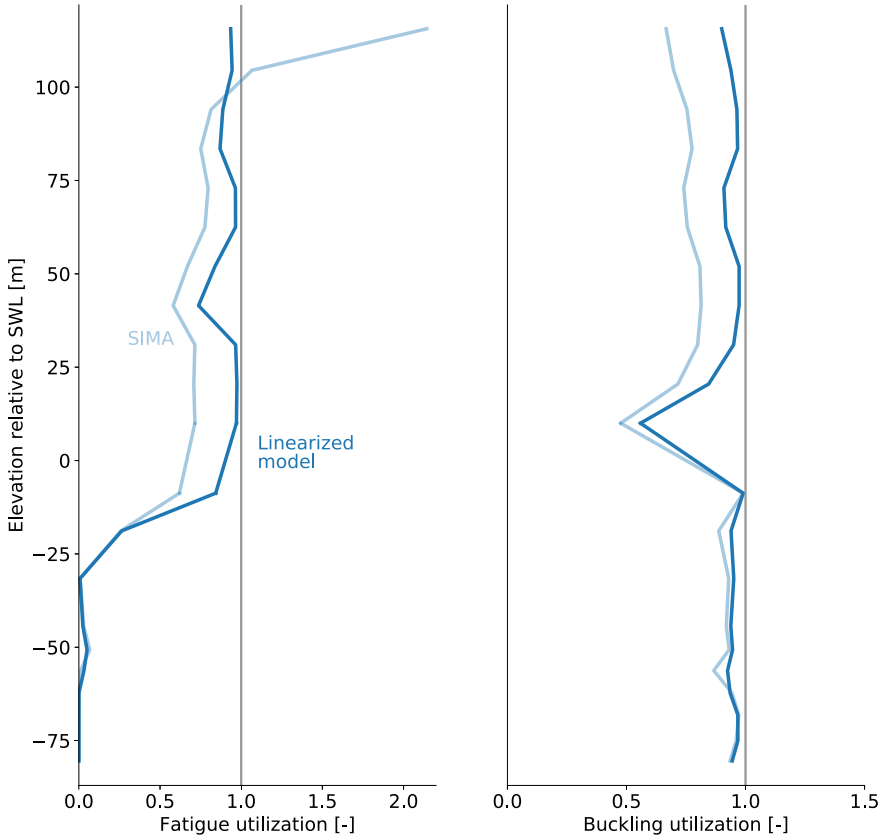

Fig. 14. Comparison of fatigue and buckling utilization factors, optimized design.

Table 9
Comparison of extreme response constraints.

Model	Initial design			Optimized design		
	Surge	Pitch	Mooring tension	Surge	Pitch	Mooring tension
Linear	35.1 m	7.0 deg	6.15×10^6 N	32.0 m	15.0 deg	5.91×10^6 N
Nonlinear	29.4 m	5.9 deg	6.68×10^6 N	27.1 m	11.3 deg	6.68×10^6 N

The platform adopts an hourglass shape below the wave zone, where the diameter is kept small to limit the wave loads on the structure. The hourglass shape maximizes the distance between the CoB and the CoG, which increases the restoring moment and natural frequency in pitch and consequently improves the behaviour in the low-frequency range for the platform pitch response. The large bottom diameter also increases the added mass in heave, which helps place the natural frequency outside the wave-frequency range.

The importance of integrated design is evident in the optimized solutions for the tower and blade-pitch control system, where the interaction with the platform clearly affects the design. For the tower, the integrated optimization results in an unconventional design where the diameter increases from the tower base, because the base diameter is constrained to match the diameter at the upper end of the platform. Varying the weight factors in the multi-objective optimization primarily affected the control system variables, which governed the trade-offs between rotor speed variation and fatigue damage in the support structure (and thus the material costs). Optimizing with fixed gains from a simple detuning procedure resulted in 0.2% higher cost and 10.5% larger rotor speed standard deviation compared to the integrated solution.

The loads on the drivetrain are not considered in the present optimization study because there is a lack of response parameters that can serve as proxies for the drivetrain performance with the current methodology. If such parameters are identified, additional terms may be included in a multi-objective optimization approach to penalize designs with unfavourable drivetrain response. As discussed in Section 3.2, finding appropriate weights for the different sub-objectives is challenging, and sensitivity studies would be needed to assess trade-offs between the variables. This would in turn increase the computational effort.

The use of linear analyses in the frequency domain imposes important limitations on the computations, since nonlinear and

transient effects are not captured. The accuracy of the model, and thus its applicability in design optimization studies, is therefore dependent on the importance of these effects. Also, the proposed methodology is only applicable for spar platforms, which limits the choices of the optimizer. A more general description of the platform geometry, which requires more comprehensive models for the hydrodynamics and structural dynamics, would allow the optimization to explore other parts of the design space and possibly identify more cost-effective solutions.

The feasibility of the optimized design is verified using state-of-the-art simulations, which show that the simplified model gives reasonably accurate predictions for both fatigue and extreme response. In general, the linearized model is conservative, especially for the platform pitch motions, which tended to be more nonlinear than the internal loads in the support structure. The main reason for the overprediction is likely to be the linearization of the aerodynamic loads.

The proposed methodology is shown to be suitable for preliminary design, where it can provide a starting design for later and more detailed design phases. The integration of several subsystems in a single design optimization process clearly affects the results and improves the overall system behaviour. The methodology can be extended to account for additional concepts, parameters, and load cases, which may help identify novel design solutions.

Declaration of competing interest

The authors declare that they have no known competing financial interests or personal relationships that could have appeared to influence the work reported in this paper.

Acknowledgements

Financial support from the Research Council of Norway (NFR) through project number 274827 - “Green Energy at Sea” is gratefully acknowledged. The first author is grateful to John Jasa for helpful discussions regarding the OpenMDAO implementation.

A. Distributed Properties for the Optimized Platform and Tower

Table 10
Distributed platform properties.

Elevation above SWL [m]	Outer diameter [m]	Wall thickness [m]
− 80.427	21.365	0.084
− 75.064	19.505	0.075
− 68.117	17.055	0.064
− 62.249	15.003	0.056
− 56.242	12.940	0.051
− 50.677	14.070	0.054
− 44.312	16.314	0.061
− 31.584	20.681	0.068
− 18.829	16.212	0.060
− 8.741	12.784	0.085
10.000	12.660	0.061

Table 11
Distributed tower properties.

Elevation above SWL [m]	Outer diameter [m]	Wall thickness [m]
10.000	12.660	0.061
20.500	14.377	0.037
31.000	14.096	0.033
41.500	13.827	0.030
52.000	12.742	0.029
62.500	11.422	0.029
73.000	10.473	0.027
83.500	9.892	0.024
94.000	8.904	0.021
104.500	7.789	0.018
115.630	6.774	0.015

B. XDSM Diagram

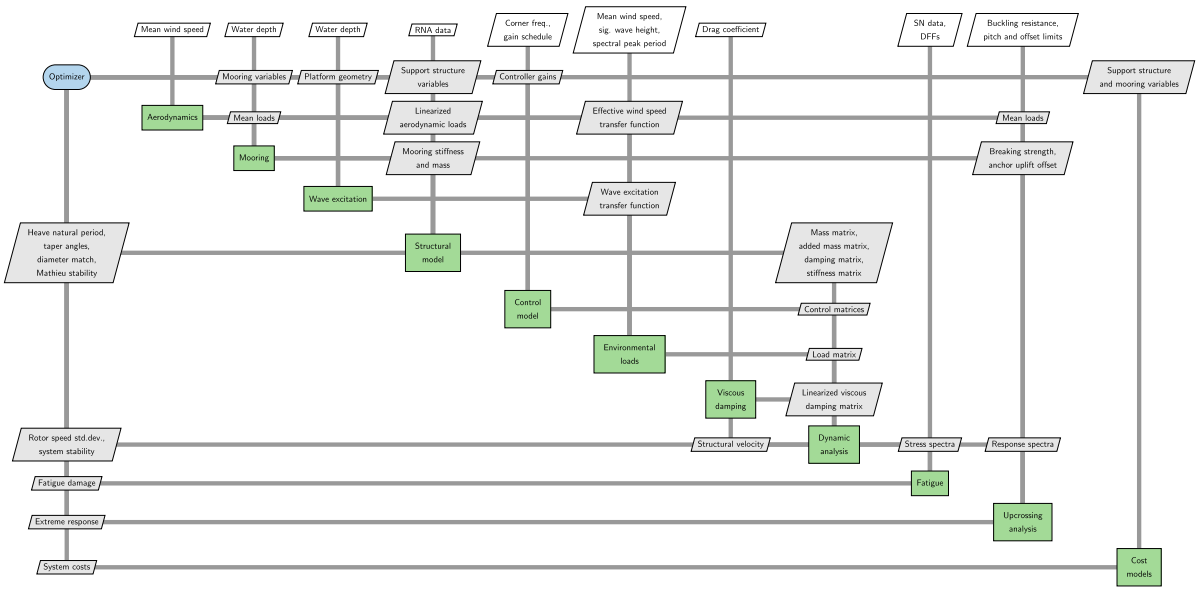

Fig. B.1. XDSM diagram showing the model layout and data dependencies. Rounded blue box is the optimizer, green boxes are analysis models, gray parallelograms are data, white parallelograms are fixed input parameters, and gray lines represent data dependencies. The data moves from top to bottom and left to right in the upper triangular part, and from bottom to top and right to left in the lower triangular part. See Lambe and Martins [42] for more details on how to interpret this figure.

References

[1] Martins JRRA, Lambe AB. Multidisciplinary design optimization: a survey of architectures. AIAA J 2013;51(9):2049–75. https://doi.org/10.2514/1.J051895.
[2] Tracy C. Parametric design of floating wind turbines. Master's thesis. Massachusetts Institute of Technology; 2007.
[3] Bachynski EE, Moan T. Design considerations for tension leg platform wind turbines. Mar Struct 2012;29:89–114. https://doi.org/10.1016/j.marstruc.2012.09.001.
[4] Gilloteaux J-C, Bozonnet P. Parametric analysis of a cylinder-like shape floating platform dedicated to multi-megawatt wind turbine. In: Proceedings of the twenty-fourth (2014) international ocean and polar engineering conference (ISOPE2014). Korea: Busan; 2014.
[5] Clauss GF, Birk L. Hydrodynamic shape optimization of large offshore structures. Appl Ocean Res 1996;18(4):157–71. https://doi.org/10.1016/S0141-1187(96)00028-4.
[6] Brommundt M, Krause L, Merz K, Muskulus M. Mooring system optimization for floating wind turbines using frequency domain analysis. Energy Procedia 2012;24:289–96. https://doi.org/10.1016/j.egypro.2012.06.111.
[7] Hall M, Buckham B, Crawford C. Evolving offshore wind: a genetic algorithm-based support structure optimization framework for floating wind turbines. In: OCEANS 2013 MTS/IEEE bergen: the challenges of the Northern dimension; 2013. https://doi.org/10.1109/OCEANS-Bergen.2013.6608173.
[8] Karimi M, Hall M, Buckham B, Crawford C. A multi-objective design optimization approach for floating offshore wind turbine support structures. J Ocean Eng Mar Energy 2017;3(1):69–87. https://doi.org/10.1007/s40722-016-0072-4.
[9] Myhr A, Nygaard TA. Load reductions and optimizations on tension-leg-buoy offshore wind turbine platforms. In: Proceedings of the twenty-second (2012) international offshore and polar engineering conference (ISOPE2012), Rhodes, Greece; 2012.
[10] Muskulus M, Schafhirt S. Design optimization of wind turbine support structures - a review. J Ocean Wind Energy 2014;1(1):12–22.
[11] Fylling I, Berthelsen PA. WINDOPT- an optimization tool for floating support structures for deep water wind turbines. In: Proceedings of the ASME 2011 30th international conference on ocean, offshore and Arctic engineering (OMAE2011), Rotterdam, The Netherlands; 2011. https://doi.org/10.1115/OMAE2011-49985.
[12] Strach-Sonsalla M, Muskulus M. Dynamics and design of floating wind turbines. In: Proceedings of the twenty-sixth (2016) international ocean and polar engineering conference (ISOPE2016), Rhodes, Greece; 2016.
[13] Tibaldi C, Hansen MH, Henriksen LC. Optimal tuning for a classical wind turbine controller. J Phys Conf 2014;555(12099). https://doi.org/10.1088/1742-6596/555/1/012099.
[14] Lemmer F, Müller K, Yu W, Schlipf D, Cheng PW. Optimization of floating offshore wind turbine platforms with a self-tuning controller. In: Proceedings of the ASME 2017 36th international conference on ocean, offshore and Arctic engineering (OMAE2017), trondheim, Norway; 2017. https://doi.org/10.1115/OMAE2017-62038.
[15] Gray JS, Hwang JT, Martins JRRA, Moore KT, Naylor BA. OpenMDAO: an open-source framework for multidisciplinary design, analysis, and optimization. Struct Multidiscip Optim 2019;59:1075–104. https://doi.org/10.1007/s00158-019-02211-z.
[16] Ashuri T, Zaaijer MB, Martins JRRA, van Bussel GJW, van Kuik GAM. Multidisciplinary design optimization of offshore wind turbines for minimum levelized cost of energy. Renew Energy 2014;68:893–905. https://doi.org/10.1016/j.renene.2014.02.045.
[17] Ashuri T, Martins JRRA, Zaaijer MB, van Kuik GAM, van Bussel GJW. Aeroservoelastic design definition of a 20 MW common research wind turbine model. Wind Energy 2016;19:2071–87. https://doi.org/10.1002/we.1970.
[18] Madsen MH Aa, Zahle F, Sørensen NN, Martins JRRA. Multipoint high-fidelity CFD-based aerodynamic shape optimization of a 10 MW wind turbine. Wind Energy Sci 2019;4:163–92. https://doi.org/10.5194/wes-4-163-2019. ISSN 23667451.

[19] Bak C, Zahle F, Bitsche R, Yde A, Henriksen LC, Natarajan A, Hansen MH. Description of the DTU 10 MW reference wind turbine. Technical Report DTU Wind Energy Report-I-0092. DTU Wind Energy; 2013.
[20] Hegseth JM, Bachynski EE. A semi-analytical frequency domain model for efficient design evaluation of spar floating wind turbines. Mar Struct 2019;64: 186–210. https://doi.org/10.1016/j.marstruc.2018.10.015.
[21] Merz K. Conceptual design of a stall-regulated rotor for a deepwater offshore wind turbine. PhD thesis. Norwegian University of Science and Technology; 2011.
[22] Bachynski EE, Etemaddar M, Kvittem MI, Luan C, Moan T. Dynamic analysis of floating wind turbines during pitch actuator fault, grid loss, and shutdown. Energy Procedia 2013;35:210–22. https://doi.org/10.1016/j.egypro.2013.07.174.
[23] Jiang Z, Karimirad M, Moan T. Dynamic response analysis of wind turbines under blade pitch system fault, grid loss, and shutdown events. Wind Energy 2014; 17:1385–409. https://doi.org/10.1002/we.1639.
[24] Larsen K, Sandvik PC. Efficient methods for the calculation of dynamic mooring line tension. In: Proceedings of the first (1990) European offshore mechanics symposium, trondheim, Norway; 1990.
[25] Lie H, Sødahl N. Simplified dynamic model for estimation of extreme anchor line tension. In: Offshore Australia, the 2nd Australian oil, gas & petrochemical exhibition and conference, Melbourne, Australia; 1993.
[26] Jonkman J, Butterfield S, Musial W, Scott G. Definition of a 5-MW reference wind turbine for offshore system development. Technical Report NREL/TP-500-38060. National Renewable Energy Laboratory; 2009.
[27] Naess A, Moan T. Stochastic dynamics of marine structures. Cambridge University Press; 2013.
[28] DNV GL. Loads and site conditions for wind turbines. Technical Report DNVGL-ST-0437. DNV GL; 2016.
[29] Dirlik T. Application of computers in fatigue analysis. PhD thesis. University of Warwick; 1985.
[30] Naess A, Gaidai O. Monte Carlo methods for estimating the extreme response of dynamical systems. J Eng Mech 2008;134(8):628–36. https://doi.org/10.1061/(ASCE)0733-9399 (2008)134:8(628).
[31] Burton T, Jenkins N, Sharpe D, Bossanyi E. Wind energy handbook. second ed. Wiley; 2011.
[32] Manwell JF, McGowan JG, Rogers AL. Wind energy explained. second ed. Wiley; 2009.
[33] Halfpenny A. Dynamic analysis of both on and offshore wind turbines in the frequency domain. PhD thesis. University College London; 1998.
[34] IEC. Wind turbines - part 1: design requirements. Technical Report IEC 61400-1. International Electrotechnical Commission; 2005.
[35] SINTEF Ocean. RIFLEX user guide. 2016.
[36] SINTEF Ocean. SIMO user guide. 2016.
[37] Jonkman BJ, Kilcher L. TurbSim user's guide: version 1.50. Technical Report NREL/TP-500-46198. National Renewable Energy Laboratory; 2009.
[38] IEC. Wind turbines - part 3: design requirements for offshore wind turbines. Technical Report IEC 61400-3. International Electrotechnical Commission; 2009.
[39] Johannessen K, Meling TS, Haver S. Joint distribution for wind and waves in the Northern North Sea. Int J Offshore Polar Eng 2002;12(1):1–8.
[40] Hwang JT, Martins JRRA. A computational architecture for coupling heterogeneous numerical models and computing coupled derivatives. ACM Trans Math Softw 2018;44(4). https://doi.org/10.1145/3182393.
[41] Martins JRRA, Hwang JT. Review and unification of methods for computing derivatives of multidisciplinary computational models. AIAA J 2013;51(11): 2582–99. https://doi.org/10.2514/1.J052184. ISSN 00011452.
[42] Lambe AB, Martins JRRA. Extensions to the design structure matrix for the description of multidisciplinary design, analysis, and optimization processes. Struct Multidiscip Optim 2012;46:273–84. https://doi.org/10.1007/s00158-012-0763-y.
[43] Gill PE, Murray W, Saunders MA. SNOPT: an SQP algorithm for large-scale constrained optimization. SIAM J Optim 2002;12(4):979–1006. https://doi.org/10.1137/S0036144504446096.
[44] Perez RE, Jansen PW, Martins JRRA. pyOpt: A Python-based object-oriented framework for nonlinear constrained optimization. Struct Multidiscip Optim 2012; 45(1):101–18. https://doi.org/10.1007/s00158-011-0666-3.
[45] Farkas J, Jármai K. Optimum design of steel structures. Springer; 2013.
[46] Teillant B, Krügel K, Guérinel M, Vicente M, Debruyne Y, Malerba F, Gradowski M, Roveda S, Neumann F, Noorloos HV, Schuitema R, Gomes R, Henriques J, Gato L, Combourieu A, Neau A, Borgarino B, Doussal J-C, Philippe M, Moretti G, Fontana M. WETFEET wave energy transition to future by evolution of engineering and technology D2.3: engineering challenges related to full scale and large deployment implementation of the proposed breakthroughs. WavEC Offshore Renewables; 2016. Technical report.
[47] Myhr A, Bjerkseter C, Ågotnes A, Nygaard TA. Levelised cost of energy for offshore floating wind turbines in a life cycle perspective. Renew Energy 2014;66: 714–28. https://doi.org/10.1016/j.renene.2014.01.017.
[48] Larsen K. Personal communication. 2019.
[49] Barltrop N. Floating structures: a guide for design and analysis. Oilfield Publications Inc.; 1998.
[50] Larsen TJ, Hanson TD. A method to avoid negative damped low frequent tower vibrations for a floating, pitch controlled wind turbine. J Phys Conf Ser 2007;75: 012073. https://doi.org/10.1088/1742-6596/75/1/012073.
[51] van der Veen GJ, Couchman IJ, Bowyer RO. Control of floating wind turbines. In: 2012 American control conference. Montreal, Canada: Fairmont Queen Elizabeth; 2012. p. 3148–53. https://doi.org/10.1109/acc.2012.6315120.
[52] Lackner M. Controlling platform motions and reducing blade loads for floating wind turbines. Wind Eng 2009;33(6):541–53. https://doi.org/10.1260/0309-524X.33.6.541.
[53] DNV GL. Fatigue design of offshore steel structures. Technical Report DNVGL-RP-C203. DNV GL; 2019.
[54] DNV GL. Floating wind turbine structures. Technical Report DNVGL-ST-0119. DNV GL; 2018.
[55] DNV. Design of floating wind turbine structures. Technical Report DNV-OS-J103. DNV; 2013.
[56] DNV GL. Buckling strength of shells. Technical Report DNVGL-RP-C202. DNV GL; 2019.
[57] Steinert A, Ehlers S, Kvittem MI, Merino D, Ebbesen M. Cost assessment for a semi-submersible floating wind turbine with respect to the hydrodynamic response and tower base bending moments using particle swarm optimisation. In: Proceedings of the twenty-sixth (2016) international ocean and polar engineering conference (ISOPE2016), Rhodes, Greece; 2016. p. 419–26.
[58] Nejad AR, Bachynski EE, Moan T. Effect of axial acceleration on drivetrain responses in a spar-type floating wind turbine. J Offshore Mech Arctic Eng 2019;141. https://doi.org/10.1115/1.4041996.
[59] DNV GL. Modelling and analysis of marine operations. Technical Report DNVGL-RP-N103. DNV GL; 2017.
[60] Koo BJ, Kim MH, Randall RE. Mathieu instability of a spar platform with mooring and risers. Ocean Eng 2004;31:2175–208. https://doi.org/10.1016/j.oceaneng.2004.04.005.
[61] Haslum HA, Faltinsen OM. Alternative shape of spar platforms for use in hostile areas. In: Offshore technology conference; 1999. https://doi.org/10.4043/10953-ms.
[62] Kreisselmeier G, Steinhauser R. Systematic control design by optimizing a vector performance index. In: International federation of active controls symposium on computer-aided design of control systems, Zurich, Switzerland; 1979. https://doi.org/10.1016/s1474-6670(17)65584-8.
[63] Lambe AB, Kennedy GJ, Martins JRRA. An evaluation of constraint aggregation strategies for wing box mass minimization. Struct Multidiscip Optim 2017;55: 257–77. https://doi.org/10.1007/s00158-016-1495-1.
[64] European Committee for Standardization. Eurocode 3: design of steel structures, part 1-6: strength and stability of shell structures. Technical Report EN 1993-1-6: 2007. European Committee for Standardization; 2007.
[65] DNV GL. Support structures for wind turbines. Technical Report DNVGL-ST-0126. DNV GL; 2018.
[66] DNV GL. Offshore mooring chain. Technical Report DNVGL-OS-E302. DNV GL; 2018.
[67] DNV GL. Position mooring. Technical Report DNVGL-OS-E301. DNV GL; 2018.
[68] Chen C-T. Linear system theory and design. fourth ed. Oxford University Press; 2013.

[69] Sandner F, Schlipf D, Matha D, Cheng PW. Integrated optimization of floating wind turbine systems. In: Proceedings of the ASME 2014 33rd international conference on ocean, offshore and Arctic engineering (OMAE2014), san Francisco, California, USA; 2014. https://doi.org/10.1115/OMAE2014-24244.
[70] Hansen MH, Henriksen LC. Basic DTU wind energy controller. Technical Report DTU Wind Energy Report-E-0018. DTU Wind Energy; 2013.
[71] Jonkman J. Definition of the floating system for phase IV of OC3. Technical Report NREL/TP-500-47535. National Renewable Energy Laboratory; 2010.
[72] Müller K, Lemmer F, Yu W. LIFES50+ D4.2: public definition of the two LIFES50+ 10MW floater concepts. Technical report. University of Stuttgart; 2018.
[73] Musial W, Butterfield S, Boone A. Feasibility of floating platform systems for wind turbines. In: 23rd ASME wind energy symposium, Reno, Nevada, USA; 2004. https://doi.org/10.2514/6.2004-1007.
[74] Lie H, Gao Z, Moan T. Mooring line damping estimation by a simplified dynamic model. In: Proceedings of OMAE 2007 26h international conference on offshore mechanics and Arctic engineering, san Diego, California, USA; 2007. https://doi.org/10.1115/OMAE2007-29155.
[75] Skaare B, Nielsen FG, Hanson TD, Yttervik R, Havmøller O, Rekdal A. Analysis of measurements and simulations from the Hywind Demo floating wind turbine. Wind Energy 2015;18:1105–22. https://doi.org/10.1002/we.1750.
[76] Saha N, Naess A. Monte Carlo-based method for predicting extreme value statistics of uncertain structures. J Eng Mech 2010;136(12):1491–501. https://doi.org/10.1061/(ASCE)EM.1943-7889.0000194.